nature communications

Article

https://doi.org/10.1038/s41467-026-68786-6

Plant fucosyltransferase FUT11 distorts the sugar acceptor to catalyze via a transient oxocarbenium intermediate mechanism

Received: 12 September 2025

Accepted: 16 January 2026

Published online: 23 January 2026

Check for updates

Víctor Taleb[1,7], Ignacio Sanz-Martínez[1,2,7], Sonia Serna[3], María Bort-Griñó[1], Yoshiki Narimatsu[4], Sanae Furukawa[4], Niels C. Reichardt[3,5], Henrik Clausen[4], Pedro Merino[1,2] ✉ & Ramon Hurtado-Guerrero[1,4,6] ✉

Glycosyltransferases catalyze glycosidic bond formation by activating the donor sugar, while the sugar acceptor substrate is considered passive, maintaining a chair conformation during catalysis. We challenge this through a multidisciplinary study of *Arabidopsis thaliana* FUT11, a core α1,3-fucosyltransferase essential for plant development and reproduction. *At*FUT11 adopts a GT-B fold with an additional N-terminal subdomain that anchors the G0 N-glycan, while the α1,3 arm is mainly recognized by the acceptor Rossmann subdomain. The α1,6 arm remains solvent-exposed, allowing diverse modifications, while solvent exposure of the central mannose's OH2 explains tolerance for β1,2-xylose. Remarkably, simulations suggest the catalytic base Glu158 may promote the innermost GlcNAc's transient puckering distortion to align the hydroxyl for nucleophilic attack. This enables an asynchronous S_N2-like mechanism bordering S_N1 character, with formation of a transient oxocarbenium ion triggered by pyrophosphate departure, followed by nucleophilic attack coupled with proton transfer. Homology with human FUT9 explains *At*FUT11's side activity on LacNAc, revealing plasticity and evolutionary convergence between plant and mammalian antenna-fucosyltransferases.

N-glycosylation is an evolutionarily conserved post-translational modification essential for the proper folding, stability, and function of glycoproteins across all domains of life[1–3]. In eukaryotes, the process is initiated in the endoplasmic reticulum (ER), where a preassembled oligosaccharide is transferred by the oligosaccharyltransferase (OST) complex to an asparagine residue within the canonical consensus sequence –Asn-X-Ser/Thr– (where X ≠ Pro) of nascent polypeptides[4]. Although most N-glycosylation events target this canonical sequon, evidence also supports the occurrence of modifications at non-consensus motifs, suggesting an unexpected degree of substrate plasticity and regulatory complexity in this pathway[5,6]. The early stages of the N-glycosylation machinery are broadly conserved, while subsequent N-glycan remodeling in the Golgi is divergent across kingdoms, contributing to the remarkable structural and functional diversity of glycoproteins[7]. Notably, in some prokaryotes, N-glycosylation pathways are even more distinct, employing distinct lipid-linked donors and OST-like enzymes to generate diverse glycan structures[3].

[1]Institute of Biocomputation and Physics of Complex Systems (BIFI), University of Zaragoza, Zaragoza, Spain. [2]Department of Organic Chemistry, Faculty of Sciences, University of Zaragoza, Zaragoza, Spain. [3]CIC biomaGUNE, Basque Research and Technology Alliance (BRTA), Donostia-San Sebastián, Spain. [4]Copenhagen Center for Glycomics, Department of Cellular and Molecular Medicine, University of Copenhagen, Copenhagen, Denmark. [5]Biomedical Research Networking Center in Bioengineering, Biomaterials, and Nanomedicine (CIBER-BBN), Donostia-San Sebastián, Spain. [6]Fundación ARAID, Zaragoza, Spain. [7]These authors contributed equally: Víctor Taleb, Ignacio Sanz-Martínez. ✉e-mail: pmerino@unizar.es; rhurtado@bifi.es

In plants, Golgi-resident glycosyltransferases further elaborate the N-glycan precursor, starting with N-acetylglucosaminyltransferase I (GnTI or MGAT1), which adds a GlcNAc residue to the α1,3Man arm that initiates complex N-glycan formation and branching[8]. In mammals, the pathway yields multi-antennary N-glycans with LacNAc units terminated by sialic acids and featuring core α1,6-linked fucose—a modification introduced by FUT8 and essential for development and immunity[9,10]. In contrast, plants generate biantennary N-glycans without sialic acids and are distinctly different by having core α1,3-fucose as well as β1,2-xylose residues attached to the innermost GlcNAc and central Man residue, respectively. These distinct plant modifications, catalyzed by the enzymes FUT11[8,11] and β1,2-xylosyltransferase (XYLT)[8,12], are immunogenic in humans and hence have implications for use of plant expressing systems for production of glycoprotein therapeutics[13]. Core fucosylation of N-glycans involves the addition of a fucose residue to the innermost N-acetylglucosamine (GlcNAc) of the N-glycan chitobiose core, but with differing linkage specificities (α1,6 in mammals versus α1,3 in plants). The β1,2-linked xylose, attached to the OH2 position of the central mannose, is a hallmark of plant N-glycans and may modulate glycoprotein folding or receptor interactions[14].

FUT11-mediated core α1,3-fucosylation is essential for normal growth, fertility, and hormone signaling in diverse plant species, as demonstrated by severe phenotypes in *Oryza sativa* and *Lotus japonicus* upon gene disruption[8,15–17]. Intriguingly, the combined loss of the FUT isoforms *FUT11* (*FucTA*) and *FUT12* (*FucTB*) in *Arabidopsis thaliana* results in no major morphological defects[18]. Despite its central role in plant N-glycosylation and its biotechnological relevance, the structural and catalytic mechanism of FUT11 remain poorly defined. The functional specificity of FUT11 was demonstrated using recombinant *At*FUT11 expressed in *Pichia pastoris*[19], and more lately evaluated by expressing *At*FUT11 in N-glycoengineered human HEK293 cells[20]. Glycan microarray screening with 18 defined N-glycan structures revealed that *At*FUT11 selectively targets complex and hybrid N-glycans with requirement for GlcNAc on the α1,3 arm. *At*FUT11 can also fucosylate N-glycans with α1,6 core fucosylation by FUT8, yielding double α1-3/6 core-fucosylated N-glycan structures[21]. This substrate tolerance was confirmed in mammalian cells co-expressing FUT8 and *At*FUT11[20].

The mechanistic borderline between S_N1 and S_N2 reactions has long been a subject of interest in carbohydrate and related chemistry, including enzymatic glycosylation reactions, in which the formation of a transient oxocarbenium ion has been proposed as a key intermediate[22] bridging the two mechanistic extremes[23]. While the S_N1 mechanism involves a fully developed glycosyl cation, and S_N2 mechanism proceeds through a concerted transition state, many reactions exhibit features of both pathways. In other words, along the continuum between S_N1 and S_N2, the latter may gradually shift towards the former as the transition state develops a carbocation character[24]. Several experimental[25] and theoretical[26] studies have addressed this continuum[27], suggesting the real formation of a glycosyl cation[28]. In glycosyltransferases, acceptor recognition is commonly discussed in terms of binding determinants and preorganization[29,30], but the possibility that these enzymes actively distort the sugar acceptor conformation has remained unexplored.

Here, we show that *At*FUT11 recognizes its *N*-glycan acceptor through a modular GT-B architecture and an acceptor-binding region organized into two subdomains, enabling selective engagement of the α1,3 arm while tolerating β1,2-xylose and conformational variability at the α1,6 arm. Using glycan microarrays, X-ray crystallography of *At*FUT11 bound to GDP and a G0 N-glycan, structure-guided mutagenesis, and multiscale computations, we identify residues contributing to donor/acceptor recognition and support an asynchronous S_N1–S_N2-like pathway in which a transient oxocarbenium-like cationic species is populated. The simulations further indicate that enzyme–acceptor interactions can promote a transient puckering distortion of the innermost GlcNAc, aligning the reactive hydroxyl for nucleophilic attack, with Glu158 implicated as a key contributor to this process. Finally, structural similarity to mammalian FUT9 provides a rationale for *At*FUT11 activity toward LacNAc in vitro, consistent with its low efficiency.

Results

*At*FUT11 substrate specificity by glycan microarray

Based on the previously described activity for this enzyme, a G0 peptide derived from chicken egg yolk sialylglycopeptide (SGP) was incubated in the presence of GDP-fucose (GDP-Fuc) with *At*FUT11 expressed in HEK293. The introduction of a fucose molecule on G0 peptide was clearly detected by MALDI-TOF mass spectrometry (Fig. 1a). As this recombinant enzyme carries mammalian-type N-glycans, the predicted sites present in our construct (Asn337, Asn420, and Asn481) map to solvent-exposed regions far from the donor/acceptor pockets (Supplementary Fig. 1a), supporting the view that heterogeneity at these sites is unlikely to affect the fucosyltransferase properties reported here. Steady-state kinetics with GDP-Fuc and the G0 acceptor showed classic Michaelis–Menten behavior, with *At*FUT11 displaying turnover rates comparable to human FUT8[31] on the GDP-Fuc/G0 pair and a modestly higher apparent K_m for GDP-Fuc but a similar K_m for G0 (Supplementary Fig. 1b).

To gain deeper insights into the substrate specificity of FUT11, we utilized an extensive collection of 144 glycan structures immobilized on microarrays with a focus on synthetic N-glycan structures (Supplementary Fig. 2)[32]. This diverse array, which encompasses a wide range of structural variability and complexity, allowed us to comprehensively assess FUT11's substrate preferences. Glycan microarrays were incubated with *At*FUT11 expressed in HEK293 in the presence of GDP-Fuc (Fig. 1b). The introduction of fucose by the action of the enzyme was detected with fluorescently labelled *Aleuria aurantia* lectin (AAL) and an antibody raised against horseradish peroxidase (anti-HRP). These reagents were chosen based on their broad recognition of fucosylated structures (AAL) and the high specificity against core α1,3 fucose N-glycans (anti-HRP)[33]. Anti-HRP reacts with β1,2-xylose-containing and core α1,3-fucosylated N-glycans, the major substituents in HRP N-glycans. As core α1,6 fucose N-glycan structures (GL64-GL71) and LDNF N-glycans (GL130 and GL131) are ligands for AAL lectin, anti-HRP was critical to distinguish core α1,3 fucosylation events. For Fig. 1b, we excluded structures that already contained core α1,3-fucose, as well as fragments lacking a chitobiose core and O-glycan-type structures, as these are not substrates for *At*FUT11. All structures included in the histograms in Fig. 1b, showed negligible recognition with AAL or anti-HRP before the reaction with *At*FUT11. After incubation with recombinant *At*FUT11, several structures printed showed the introduction of fucose as determined by the successful interactions with one of the two fucose recognizing reagents. The minimal structure that supported fucosylation was GL49, a truncated structure that only presents the α1,3 arm with a terminal GlcNAc in agreement with our previous results[21].

The presence of β1,2-xylose was tolerated by *At*FUT11 (GL3), and core α1,6-fucosylated N-glycans were also efficiently fucosylated, consistent with earlier results. Even highly branched α1,6 arms (GL50, GL54) did not significantly affect substrate recognition. N-glycans bearing β1,4-galactose on the α1,3 arm were accepted as substrates (GL59, GL126), whereas the presence of β1,4-GalNAc, Lewis^X, or LDNF epitopes on the α1,3 arm (GL128, GL92, GL130) impaired *At*FUT11 activity. These results refine our understanding of the structural requirements for *At*FUT11 substrate recognition and are largely consistent with previous reports.

Architecture of the *At*FUT11-GDP-G0 complex

To explain *At*FUT11's preferences for the N-glycans described above, we successfully obtained $P2_1$ crystals of *At*FUT11 bound to GDP and G0

https://doi.org/10.1038/s41467-026-68786-6

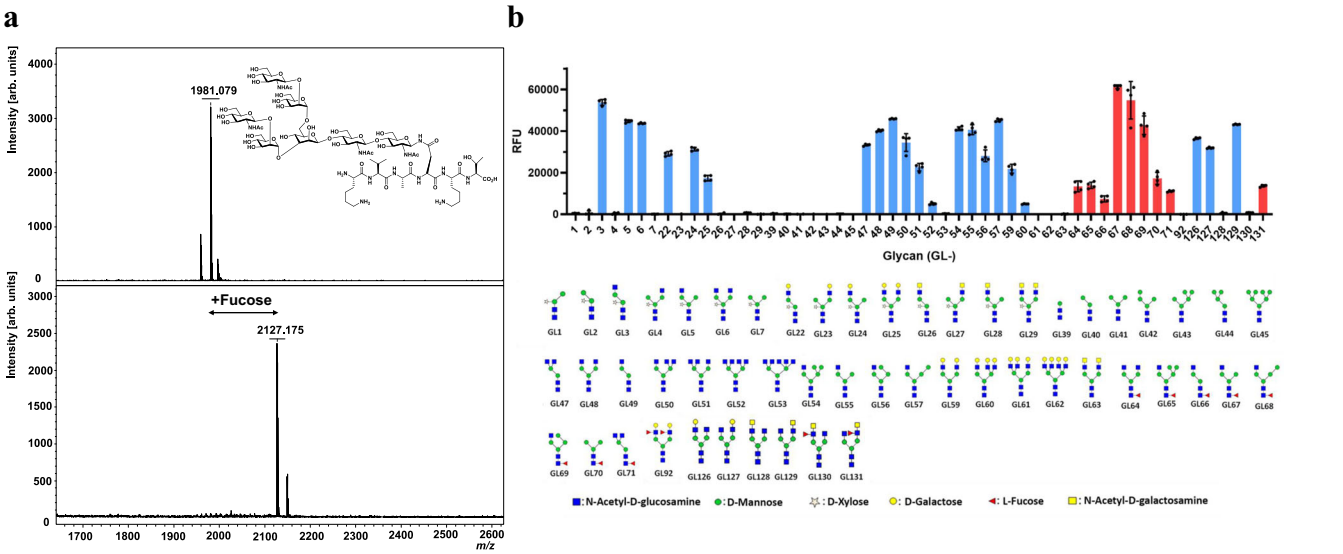

Fig. 1 | Activity assay of *At*FUT11 in solution and on glycan microarray. a Activity of *At*FUT11 on G0 glycopeptide. MALDI-TOF spectra of the G0 glycopeptide (up) and after the action of recombinant *At*FUT11 showing the introduction of fucose on G0 (down). **b** (upper panel) Activity of recombinant *At*FUT11 on glycan microarrays. After reaction with *At*FUT11, introduced fucose on individual spots was revealed with L-fucose recognizing reagents, *Aleuria aurantia* lectin (AAL) (blue) and Anti-horseradish peroxidase Anti-HRP (red). Each histogram represents the Mean of relative fluorescence units (RFU) values +/− SD (standard deviation) for replicates spots (black dots, $n = 4$). (Lower panel) N-glycan structures represented in the histograms. Source data are provided as a Source Data file. In particular, the source data for Fig. 1b contains relative fluorescence units (RFU) data for each individual spot for each glycan printed in the microarrays before and after incubation with *At*FUT11, detected with fluorescent *Aleuria aurantia* lectin and Anti-HRP antibody. Data reported are from a single representative experiment; the experiment was independently performed twice to confirm reproducibility.

N-glycan (Table 1). These crystals enabled structure determination at high resolution (1.41 Å) and clear interpretation of the electron density map (Table 1). As expected, structural comparison using the DALI server[34] revealed homology to other α1,3-FUTs, including mango FUT13 (PDB entry 7YRO[35]), human FUT9 (PDB 8D0Q, 8D0W, 8D0U, 8D0P, and 8D0R[36]), and *Helicobacter pylori* FUT (PDB 2NZX, 2NZY, 2NZW[37]). Although *At*FUT11 differs substantially from these enzymes in acceptor specificity, the superpositions yielded good structural alignments (RMSDs of ~2.9 to ~3.4 Å over 297–338 aligned residues), indicating a conserved fold.

The structure of *At*FUT11 in complex with GDP and G0 reveals an unusual GT-B architecture. The donor domain (residues 201–347) adopts a canonical Rossmann fold that coordinates GDP-Fuc. The acceptor domain comprises an N-terminal subdomain (residues 88–200) and a second Rossmann fold subdomain (residues 348–501). These subdomains are covalently connected by three disulfide bridges (C91–C391, C124–C326, and C128–C367; Fig. 2a) and engage in close intramolecular interactions. Notably, the N-terminal subdomain is distinct to *At*FUT11 and is absent from other α1,3-FUTs (Fig. 2a). The electron densities for both GDP and the G0 glycan are well resolved (Fig. 2b). However, interestingly, the electron density for the innermost GlcNAc (A^{G0}) is only partially defined, which may reflect either intrinsic flexibility of this sugar moiety, or—as shown below—be compatible with a transient conformational distortion away from its canonical chair geometry within the enzyme–substrate complex that could facilitate catalysis. In contrast to FUT8, where the G0 chitobiose core adopts an anti-ψ conformation[9], the G0 in *At*FUT11 assumes the more stable syn-ψ conformation[38] (Fig. 2b), specifically affecting the GlcNAcβ1,4GlcNAc linkage between A^{G0} and B^{G0} units.

The structure further reveals that GDP is solvent-exposed and located exclusively within the donor domain, while the majority of the G0 glycan is anchored in the N-terminal subdomain. The α1,3 arm of the N-glycan is positioned within the Rossmann subdomain, while the α1,6 arm remains exposed to solvent (Fig. 2c). This suggests that the N-terminal subdomain, together with the second Rossmann subdomain, forms the N-glycan binding site, facilitating G0 recognition. Unlike proper exosites that can also recognize N-glycans and are found in other FUTs such as FUT8[9] and the more distantly related MGAT2[39], the N-terminal subdomain in *At*FUT11 is not a true exosite, as it also provides the catalytic base (see below).

Recognition of GDP-Fuc in the donor site of *At*FUT11

The active site of *At*FUT11 is large, accommodating both the GDP-Fuc and N-glycan (Fig. 3a). The guanosine moiety of GDP-Fuc is anchored via hydrogen bonds involving the side chains of Ser218, Arg248, Lys256, and Glu280, as well as the backbone of Phe216. The pyrophosphate group is stabilized by interactions with the backbones of Ser218 and Asn219, and the side chains of Asn219, Arg226, Asn271, and Lys281. The enrichment of positively charged residues such as Arg226 and Lys281 is a characteristic feature of GT-B fold glycosyltransferases, which do not require metal ions for activity[40]. These basic residues substitute for the divalent metal ions typically used by GT-A fold enzymes, helping stabilize the pyrophosphate and ensuring the correct positioning of the sugar nucleotide for catalysis[40].

To gain structural insight into the catalytic mechanism, we modeled GDP-Fuc into the donor site using coordinates from *Hp*FUT complexed with GDP-Fuc (PDB entry: 2NZY)[37]. The resulting *At*FUT11–GDP-Fuc–G0 ternary complex shows that Glu158 is positioned near the OH3 group of A^{G0}, the acceptor hydroxyl targeted for fucosylation, suggesting a key role in catalysis (Fig. 3a, b). This arrangement provides the structural foundation to explore the reaction mechanism described below.

Molecular recognition of the G0 N-glycan by *At*FUT11

A^{G0} is anchored via hydrogen bonds between its carbonyl group and the side chain of Tyr163, and between its OH3 group and Glu158. B^{G0} is stabilized through interactions involving its OH6 group and the side chains of Glu158 and Tyr192. The adoption of the more stable syn-ψ conformation by the A^{G0}–B^{G0} chitobiose core is essential, as it orients the A^{G0} OH3 group towards GDP-Fuc, enabling fucosylation (Fig. 3a, b). The branching sugars of G0 (C^{G0}, F^{G0}, and G^{G0}) are positioned within the N-terminal subdomain, while D^{G0} and E^{G0} are recognized by both

Table 1 | Data collection and refinement statistics

	*At*FUT11-GDP-G0
Data collection	
Space group Wavelength (Å)	$P2_1$ 0.9791
Cell dimensions	
a, *b*, *c* (Å) α, β, γ (°)	77.66, 41.15, 82.42 90, 96.89, 90
Number of protein molecules per asymmetric unit	1
Resolution (Å)	20.00-1.41 (1.49–1.41)[a]
Rpim	0.034 (0.829)
I / σI	6.5 (0.7)
Completeness (%)	94.3 (83.1)
Redundancy	2.8 (2.6)
Mn(I) half-set correlation CC(1/2)	0.999 (0.662)
Refinement	
Resolution (Å)	1.41
Total number of reflections	266,804
Total number of unique Reflections	94,108
R_{work} / R_{free}	0.204/0.2284
No. of atoms	
Protein	3330
GDP	28
G0	90
Waters	280
B-factors (Å^2)	
Protein	32.39
GDP	19.50
G0	36.20
Waters	34.92
R.m.s. deviations	
Bond lengths (Å)	0.0090
Bond angles (°)	1.784

One crystal was used to determine the crystal structure.
[a]Values in parentheses are for highest-resolution shell.

subdomains (Fig. 3a). C^{G0} OH4 forms a hydrogen bond with the side chain of Glu197, and F^{G0} OH6 interacts with the backbone of Glu197. G^{G0} (the GlcNAc on the α1,6 arm) is fully solvent-exposed and does not interact with the enzyme. This limited recognition of the α1,6 arm likely accounts for the greater substrate tolerance observed at this branch. In contrast, the α1,3 arm is tightly recognized. D^{G0} OH3 forms a hydrogen bond with the side chain of His361, OH4 with Asp120, and OH6 with Met157. Similarly, E^{G0} OH1 interacts with His361, its carbonyl group contacts both the side chain and backbone of Ser362, and OH3 forms a hydrogen bond with the backbone of Ala358. His361 also establishes a CH–π interaction with E^{G0}, contributing further to binding. These extensive contacts with E^{G0} rationalize the strict requirement for a GlcNAc moiety at this position, as it enhances α1,3 arm recognition and stabilizes the entire glycan in the bound state. Additional sugars can be tolerated at E^{G0} OH4 and OH6, as these hydroxyls are solvent-exposed (Fig. 3c). Likewise, C^{G0} OH2 is solvent-accessible, explaining *At*FUT11's tolerance for β1,2-xylose at this site. A^{G0} OH6 is also exposed, allowing the enzyme to accommodate core α1,6-fucosylation (Fig. 3c). However, it remains unclear why *At*FUT11 does not tolerate GalNAc moieties at the E^{G0} position, while Gal residues are accepted.

*At*FUT11 mutant analysis in glycoengineered HEK293 cells

To dissect the functional importance of specific residues in *At*FUT11, we designed four alanine single-substitution mutants—E158A, Y192A, E197A, and H361A—based on structural analysis of the enzyme in complex with GDP and G0 N-glycan. Glu158 was predicted to function as the catalytic base due to its hydrogen bond to the hydroxyl group of the innermost GlcNAc acceptor, while the other residues are involved in G0 substrate binding. We assessed the catalytic ability of *At*FUT11 wild-type enzyme and these mutants by introducing the full coding constructs of *At*FUT11 and those variants via targeted knock-in (KI) in a genetically engineered HEK293 cell line (HEK293^{Biantennary}) that lacks multiple endogenous glycosyltransferases involved in various steps of N-glycosylation biosynthesis (capping by ST3GAL4/6, ST6GAL1, FUT4, elongation by B4GALNT3/4, and branching by MGAT3/4 A/4B/5, and FUT8) (Fig. 4a). This glycoengineered background, displaying simplified biantennary N-glycans as substrates, provided a clean slate to evaluate the activity of introduced *At*FUT11 variants without interference from competing glycosylation pathways, as previously described[20]. Importantly, the *FUT8* gene, which catalyzes the α1,6 core fucosylation on the same core GlcNAc residue, was deleted. Each *At*FUT11 variant (wt and mutants) was integrated individually into the AAVS1 safe harbor locus using ZFN-mediated targeted KI and the clones were validated by junction PCR to confirm proper integration of the gene (Supplementary Fig. 3). To quantify the α1,3-fucosylation activity, we then employed flow cytometry using an α1,3-fucose-specific polyclonal antibody. As shown in Fig. 4b, wild-type *At*FUT11 expressed in HEK293^{Biantennary} clearly exhibited α1,3-fucosylation, with no detectable α1,6-fucosylation as confirmed by staining with *Lens culinaris* agglutinin (LCA) lectin. This absence of α1,6-fucosylation across all KI mutant cell lines validates the KO of *FUT8* in the cell background and further supports the specificity of α1,3-fucosylation by *At*FUT11. The E158A mutant completely abolished enzymatic activity, consistent with its predicted role as the catalytic base. Mutations at Tyr192 and Glu197 resulted in only minimal α1,3-fucosylation, likely due to impaired acceptor substrate binding or disruption of the precise orientation of the innermost GlcNAc required for catalysis. In contrast, the H361A mutant retained activity comparable to the wild-type enzyme, indicating that His361 is not essential for catalytic function. This observation is further supported by molecular dynamics simulations, which show that His361 does not form stable interactions with the α1,3 arm of the *N*-glycan, reinforcing its dispensability for substrate engagement and enzymatic turnover (Supplementary Fig. 4).

Prompted by these findings, we sought to provide a molecular explanation for the functional redundancy between *At*FUT11 and its isoform, *At*FUT12. As previously reported, *At*FUT12 shares high sequence identity with *At*FUT11 and displays overlapping enzymatic activity in heterologous expression systems, including mammalian cells engineered to express biantennary N-glycans and core α1,6-fucosylation machinery[20]. An alignment of their protein sequences reveals that residues critical for donor and acceptor binding—including the catalytic base Glu158 and G0-binding residues Tyr192 and Glu197—are strictly conserved (Supplementary Fig. 5). This high degree of active site conservation provides a clear rationale for their overlapping activity[20] and validates the use of *At*FUT11 as a representative model for this enzyme class.

Collectively, this cellular assay confirmed the catalytic role of Glu158, highlighted additional residues crucial for activity, and linked our structural insights with both in-cell functional readouts and the known isoform redundancy in *Arabidopsis*.

Dynamic behavior and sugar puckering in *At*FUT11

Molecular dynamics (MD) simulations of the Michaelis complex (MC) revealed notable ligand instability, especially in the acceptor substrate. Comparative analyses, including simulations with positional restraints, showed that interactions between Glu158 and the A^{G0} subunit are crucial for maintaining complex integrity. These interactions are consistent with a transient conformational distortion of the innermost GlcNAc unit in G0. To characterize this distortion, conformational

https://doi.org/10.1038/s41467-026-68786-6

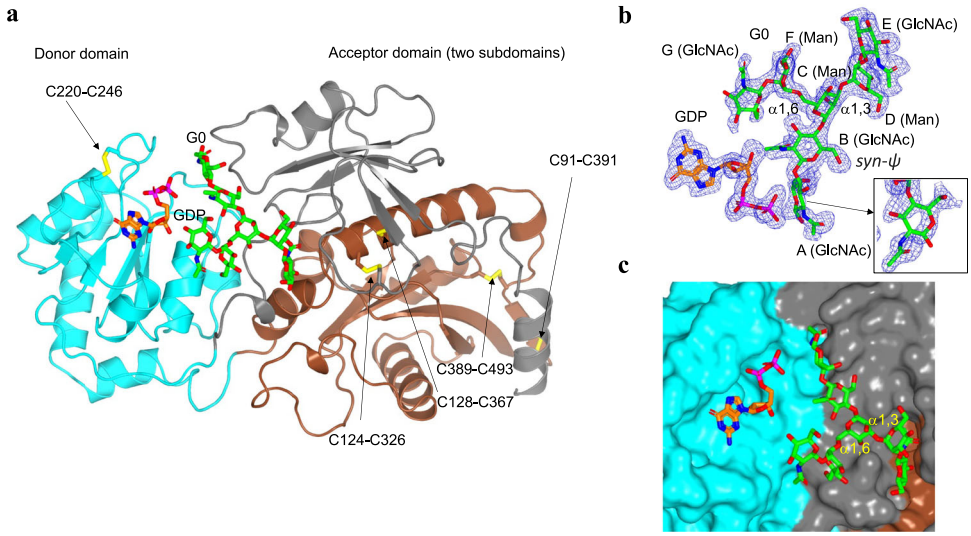

Fig. 2 | Overall structure of AtFUT11 complexed to GDP and G0. a Ribbon structure of *At*FUT11 with GDP (orange carbon atoms) and G0 (green carbon atoms). The donor domain, and the N-terminal and the Rossmann subdomains are colored in cyan, gray and brown, respectively. Disulfide bridges are indicated as yellow sulfur atoms. **b** Electron density maps are F_O–F_C (blue) contoured at 2.2σ for GDP and G0. The labels of the sugar units (A–G) are also shown. The panel highlighted by the black dashed box shows a close-up view of sugar unit A (GlcNAc) in an alternative viewing orientation to better illustrate the electron density around this residue. **c** Surface representation of the *At*FUT11-GDP-G0 complex.

analysis was conducted on the A^{G0} and fucose moieties. In the MC context, the A^{G0} subunit adopts a distorted $^1S_3$-like minimum (see below).

Given the well-known limitations of classical force fields (FFs) in accurately describing sugar flexibility[41], hybrid QM/MM/MD simulations were performed to more accurately capture the structural and electronic features relevant for substrate recognition and catalysis. These simulations confirmed that several interactions observed in the crystal structure persist throughout the trajectory. Glu280 and Ser218 consistently interacted with the guanosine moiety of GDP-Fuc, while the diphosphate group remained stably bound to Lys281 and Arg226. Additional contacts were observed between Thr272, Glu270, and Tyr162 and the hydroxyls of the fucose unit.

Conversely, interactions involving Arg248, Phe219, Tyr163, Asn219, and Asn271 were not retained; instead, new contacts formed between the main chains of Val254 and Gly252 and the guanine base. This shift may be due to the fucose moiety modifying the interaction landscape as the complex approaches the reactive state (Fig. 5a and Supplementary Fig. 6).

Consistent interactions were also observed between Ser362, Asp120, Glu197, Tyr192, and Glu158 and the E, D, C, B, and A subunits of the acceptor, respectively (Fig. 5a and Supplementary Fig. 6). Additionally, further interactions emerged involving the α1,3-arm of the glycan, particularly between Ser194 and the backbone of Gly191 with the E^{G0} subunit. In contrast, His361 did not form stable interactions in any simulation, consistent with the catalytic activity retained in the H361A mutant, indicating it is dispensable for α1,3-arm recognition (Supplementary Fig. 4). To probe the reactive conformation, distance restraints were applied to approximate the pre-glycosylation state. Under these conditions, the fucose unit favored a canonical $^1C_4$ conformation (Supplementary Fig. 7), while A^{G0} adopted a single minimum resembling a B_{3O}-$^1S_3$-like conformation, optimally orienting the OH3 group for nucleophilic attack and proton transfer (Fig. 5b).

When restraints were removed (MC), two minima emerged: one B_{3O}-like (as in RE) and another $^1S_5$-like. This shift results from the substitution of the OH3–base hydrogen bond by a conserved interaction between OH3 and the GDP-Fuc pyrophosphate, leading to A^{G0} reorganization, as supported by metadynamics (Supplementary Fig. 8).

To assess donor-induced effects, conformational studies were conducted on *At*FUT11–G0–GDP (trimer) and *At*FUT11–G0 (dimer). The trimer retained both energy minima seen in the MC, with minor free energy landscape (FEL) changes likely due to increased flexibility in the absence of fucose. In contrast, the dimer favored $^1S_5$–$^OS_2$-like states, likely due to the absence of stabilizing interactions between A^{G0} and the diphosphate group (Supplementary Fig. 9). Finally, the role of Glu158 in conformational activation was confirmed through simulations of the E158A mutant, which favored a single $^4C_1$ chair conformation, typical of unstrained GlcNAc residues. These findings underscore the dual role of Glu158: acting not only as the catalytic base but also as a conformational effector, potentially promoting distortion of the acceptor GlcNAc into a reactive conformation that could facilitate catalysis (Fig. 5c).

Mechanistic insights into the fucosyl transfer reaction

QM/MM/MD simulations revealed a preferential interaction between the OH3 group and the pyrophosphate moiety of GDP-Fuc. To assess the feasibility of OH3 activation, we investigated the transition from the Michaelis complex (MC) to the reactive state (RE). Metadynamics simulations successfully bridged these conformations, revealing an energy difference of ~2.5 kcal/mol between MC and RE, with a transition barrier below 7 kcal/mol (Supplementary Fig. 10). Taken together, these low energetic requirements, along with the spontaneous OH3 exchange observed in the QM/MM/MD trajectories (Supplementary Fig. 6), are consistent with a rapid, dynamically exchanging process.

Using a representative minimum-energy structure from the puckering analysis of the A^{G0} moiety with soft restraints (Fig. 5b), the free energy surface (FES) for the fucosyl transfer reaction was computed based on two collective variables:

$$CV1 = d_1 - d_2 \quad (1)$$

representing glycosyl transfer such as the difference between the glycosidic bond that is broken (d_1) and the one that is formed (d_2), and

$$CV2 = d_3 - d_4 \quad (2)$$

https://doi.org/10.1038/s41467-026-68786-6

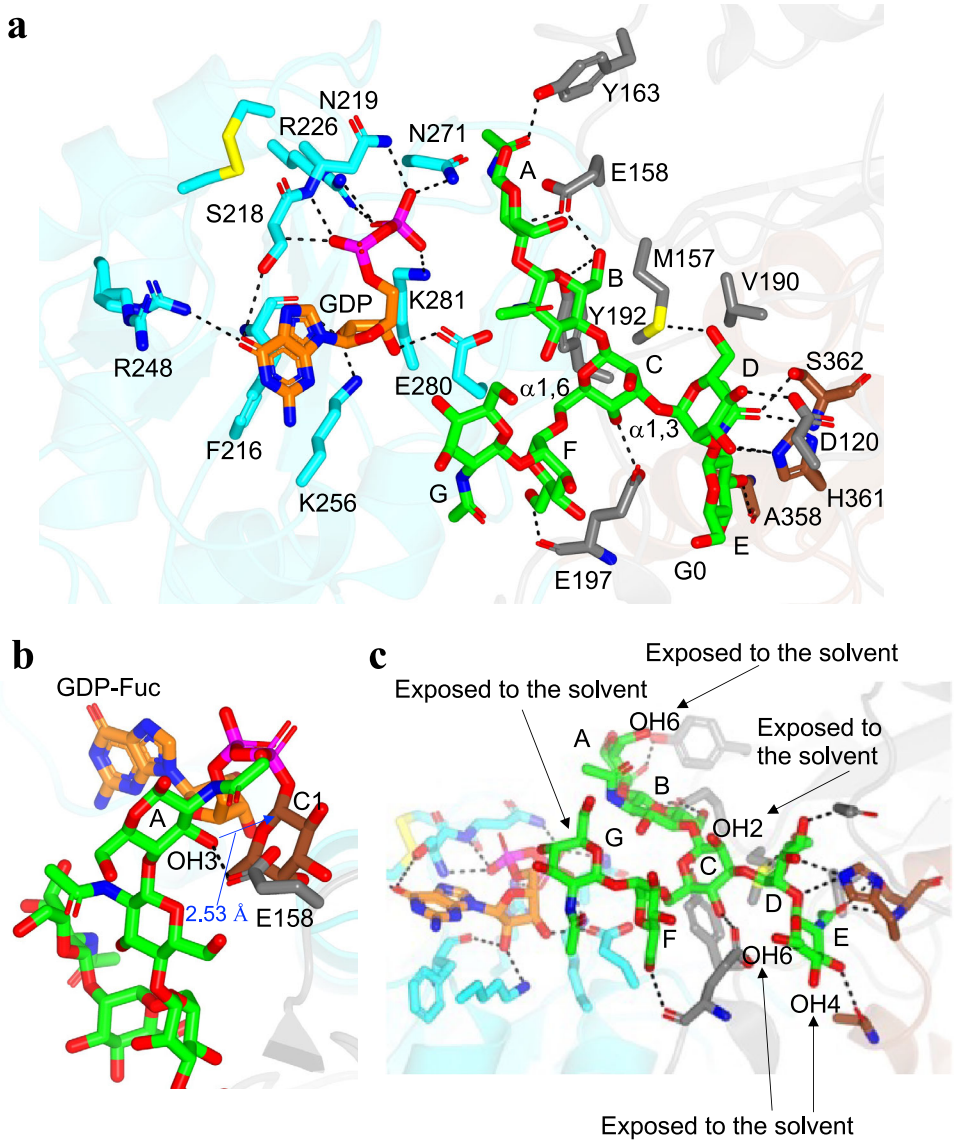

Fig. 3 | Structural features of GDP-Fuc and G0 binding sites. a Complete GDP-Fuc and G0 binding sites of the *At*FUT11-GDP-G0 complex. The residues forming the GDP-Fuc and G0 binding sites follow same colors described above. GDP and G0 are shown as orange and green carbon atoms, respectively. Hydrogen bond interactions are shown as dotted black lines. **b** Close-up view of the binding site region of the *At*FUT11-GDP-Fuc-G0 complex showing the position of the catalytic base Glu158 with respect to the anomeric carbon of GDP-Fuc in the plausible S_N2 single-displacement reaction mechanism. Note the proximity and the orientation of the A^{G0} OH3 to the anomeric carbon (2.53 Å) which is compatible with the inversion of the configuration during the reaction. **c** Close-up view of the G0 binding site region, highlighting the hydroxyl groups on specific sugar units that are exposed to the solvent.

describing proton transfer as the difference between the O–H bond that is broken in the nucleophile (d_3) and the one that is formed in the catalytic base (d_4) (Fig. 6a). Each point on the FES reflects a discrete stage along the reaction coordinate (with the X-axis corresponding to C1–O3 bond formation and the Y-axis to proton transfer from OH3 to Glu158). Free energy surface (FES) analysis revealed two local minima corresponding to the reactant (RE) at CV1 ≈ −1.49 Å and CV2 ≈ −0.91 Å, and the product (PR) at CV1 ≈ 1.46 Å and CV2 ≈ 0.94 Å (Supplementary Fig. 11). The calculation of the minimum free-energy path (MFEP), which can be considered as an equivalent of the well-known intrinsic reaction coordinate (IRC) revealed a transition state (TS) located at CV1 ≈ 0.43 Å and CV2 ≈ −0.64 Å (Fig. 6b and Supplementary Fig. 11). The transition-state nature of this TS was confirmed through a committor analysis[42], which showed that the system relaxed almost equally toward RE and PR (see 10.5281/zenodo.17558724). The calculated activation barrier from the Michaelis complex was ~18.5 kcal mol^{-1}, in agreement with values reported for other fucosyltransferases (17–20 kcal·mol^{-1})[43,44], and consistent with our experimental results. The studied reaction is exergonic by 0.4 kcal/mol, which reflects a thermodynamically slightly favored process. However, it must be considered that the molecular process analyzed leads to a product (PR) in which the catalytic base (E158) remains protonated. It is reasonable to assume that this PR product would promptly exchange a proton with the surrounding aqueous medium, thereby regenerating the catalytic base and allowing the catalytic cycle to restart (For a proposed catalytic cycle, see Supplementary Fig. 12).

Closer inspection of the FES topology reveals a flat region beyond the TS, which may be indicative of the presence of a transient intermediate or, at least, of a transient meta-stable situation, as reflected by a small shoulder, characteristic of such scenarios in non-enzymatic reactions[26,45,46], along the corresponding MFEP represented in Fig. 6b.

Interatomic distances at the TS (d_4 ≈ 1.6 Å; d_3 ≈ 1.0 Å) indicate an asynchronous mechanism, where proton transfer occurs after the TS, consistent with a late transition state and an associative reaction

https://doi.org/10.1038/s41467-026-68786-6

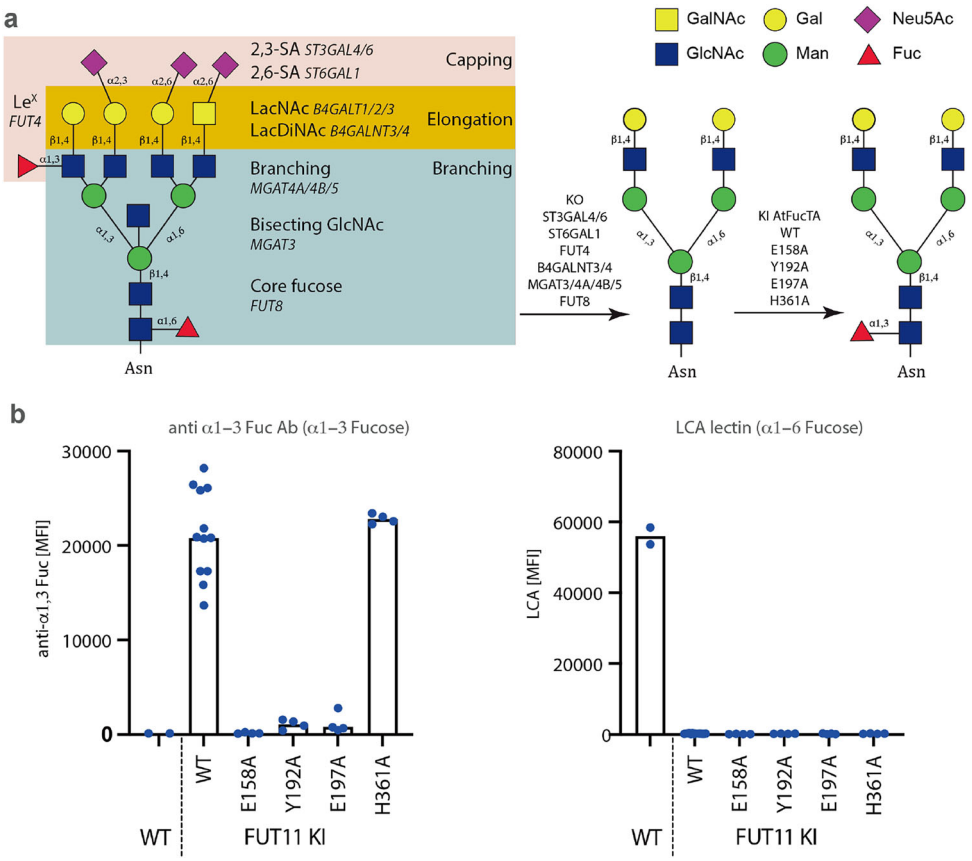

Fig. 4 | Flow cytometry analysis of the reinstallation of α1,3 fucose with *At*FUT11 WT and mutants. a The N-glycosylation pathway is indicated with the name of the enzymes involved in the synthesis of N-glycan structures in HEK293 cells. The engineering strategy to develop HEK293 biantennary clone was performed with multiple gene KOs of ST3GAL4/6, ST6GAL1, FUT4, B4GALNT3/4, MGAT3/4A/4B/5 and FUT8 followed by the individual targeted KI of *At*FUT11 WT and 4 mutants. **b** (Left panel) Flow cytometry analysis using an α1,3-fucose-specific polyclonal antibody to assess cell surface expression of the α1,3-fucosylated glycoform in HEK293WT (WT) and FUT11 KI clones expressed in HEK293^{Biantennary} cells. (Right panel) Flow cytometry analysis using LCA lectin, which specifically binds to α1,6-fucosylated glycans. Bar graphs represent the average mean fluorescence intensity (MFI) from two independent experiments. Analysis was gated on the live cell population based on forward and side scatter area (FSC-A and SSC-A), and doublets were excluded using forward scatter and width (FSC-H and FSC-W). Each experiment included at least two clones per *At*FUT11 knock-in variant ($n = 14$ for *At*FUT11 wild-type, and $n = 4$ for each individual alanine mutant, except E197A, which had $n = 6$). All clones analyzed by flow cytometry were previously validated by junction PCR to confirm correct integration of the gene into the AAVS1 safe harbor locus (see Supplementary Fig. 3). Source data are provided as a Source data file.

profile. Close inspection of the residues surrounding the transition structure shows stabilizing electrostatic interactions between the pyrophosphate group and Arg226, Lys281, and Ser218, which collectively facilitate GDP departure. At this point, the fucose adopts a $^3H_4$-like conformation (Fig. 6c). Non-covalent interaction (NCI)[47,48] analysis of the transition structure further confirms that proton transfer has not yet taken place, supporting the asynchronous nature of the process (Fig. 6d). In fact, in the MFEP-based reaction movie, we observe features consistent with a short-lived oxocarbenium-like species (Supplementary Movie 1).

To gain deeper insight into the electronic rearrangements along the reaction coordinate, we performed an Electron Localization Function (ELF)[49,50] analysis on representative snapshots along the MFEP, which connects the RE and product PR states through the TS. The Electron Localization Function (ELF) enables the visualization of changes in electron density through entities known as attractors, which correspond to local maxima within specific spatial regions called basins (disynaptic when shared between two atoms or monosynaptic when belongs to one atom). By observing how these attractors shift, it becomes possible to determine the precise moment when a bond is formed or broken, or when an atom gains or loses an electron pair. Accordingly, distinct stages (or events) of a reaction can be defined, independent of the number of reaction steps, which are determined by the corresponding kinetics. By defining these stages, temporally stable situations may arise with significant implications, such as stereochemical consequences. These situations may exhibit an appreciable lifetime without constituting local energy minima, and thus cannot be considered true intermediates but transient intermediates[26,45,46]. While ELF analysis has proven effective for characterizing transient intermediates computationally[51–53], its application to enzymatic reaction mechanisms remains relatively rare in the literature[54–57].

In the FUT11-catalyzed reaction, we initially performed an ELF analysis along the MFEP (Fig. 6b) represented in Fig. 6e (for the populations of the basins in each point see Supplementary Table 1). It can be clearly observed how the C1–OP bond starts to break at the beginning of the process (point 9, Fig. 6f) and is fully cleaved by point 13, at which point neither the nucleophilic attack of O3 nor the OH3 group transfer has yet occurred. Therefore, we can state that from this point onwards, a glycosyl cation is formed, though it would be more accurate to describe it as an intimate ion pair. However, this species cannot be localized as an energy minimum and must be classified as a transient intermediate, and thus it does not represent a proper reaction step. What is certain is that this situation persists until point 67 (Fig. 6f), where hydrogen transfer begins, almost simultaneously with the onset of C1–O3 bond formation. Finally, the bond is formed, and the OH3 group is transferred (point 74, Fig. 6f). In summary, according

https://doi.org/10.1038/s41467-026-68786-6

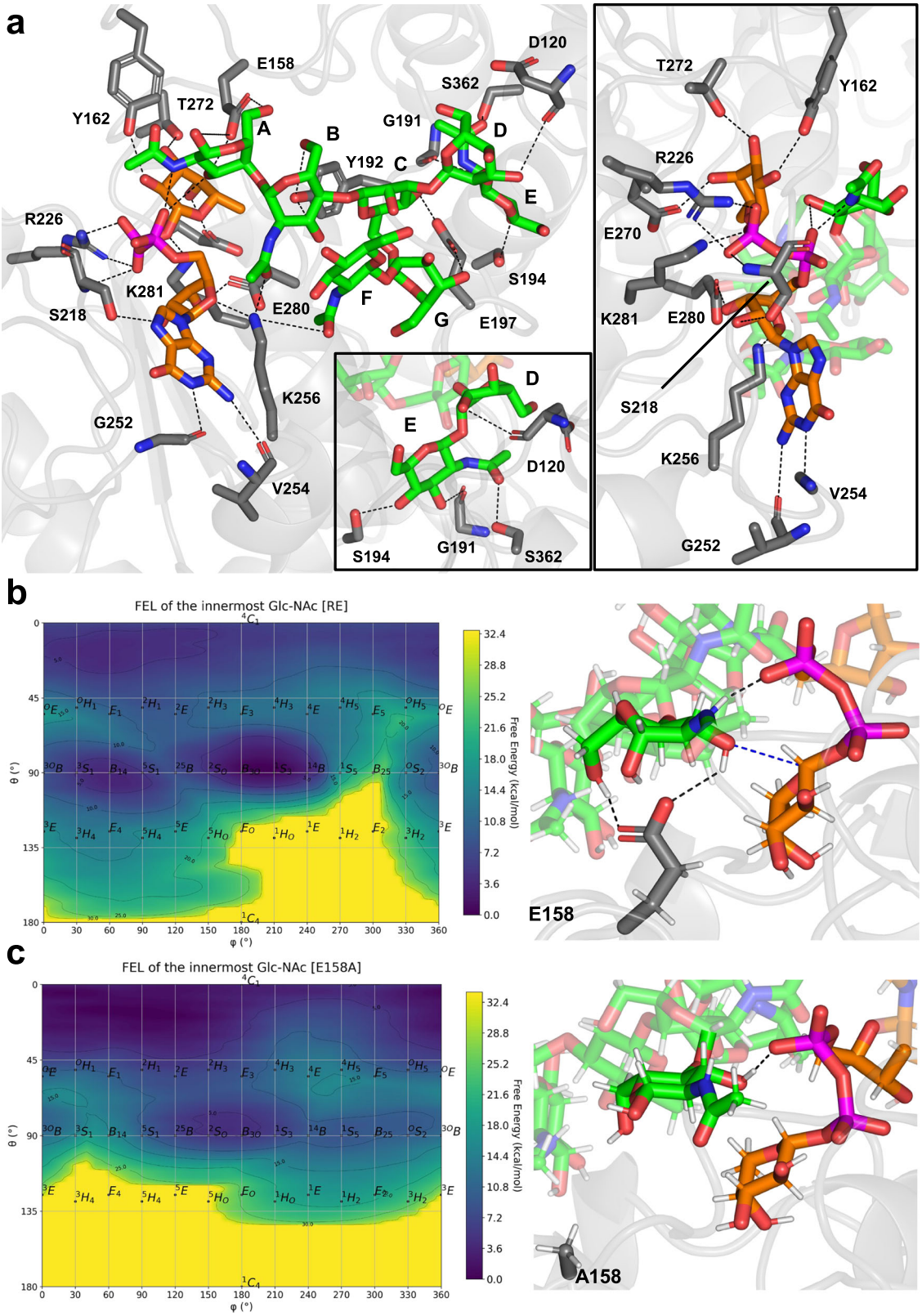

Fig. 5 | Dynamic behavior and sugar puckering in AtFUT11. a Key conserved interactions observed during QM/MM/MD simulations of the Michaelis complex (MC). For clarity, hydrogen atoms are omitted. Residues forming persistent interactions with the GDP-Fuc and the G0 acceptor are labeled. **b** Free energy landscape (FEL) of the innermost GlcNAc unit under conformational restraints mimicking the geometry of the reactive species. The inset shows a representative structure of the conformational minimum adopted by the A^{G0}, characterized by a B_{3O}–$^{1}S_{3}$-like pucker. **c** Free energy landscape of the innermost GlcNAc unit in the E158A mutant, illustrating the loss of conformational distortion. The inset displays a representative structure corresponding to a canonical $^{4}C_{1}$ conformation. In all panels, *At*FUT11 carbon atoms are shown in gray, the G0 glycan in green, and the GDP-Fuc donor in orange. Source data are provided as a Source data file.

https://doi.org/10.1038/s41467-026-68786-6

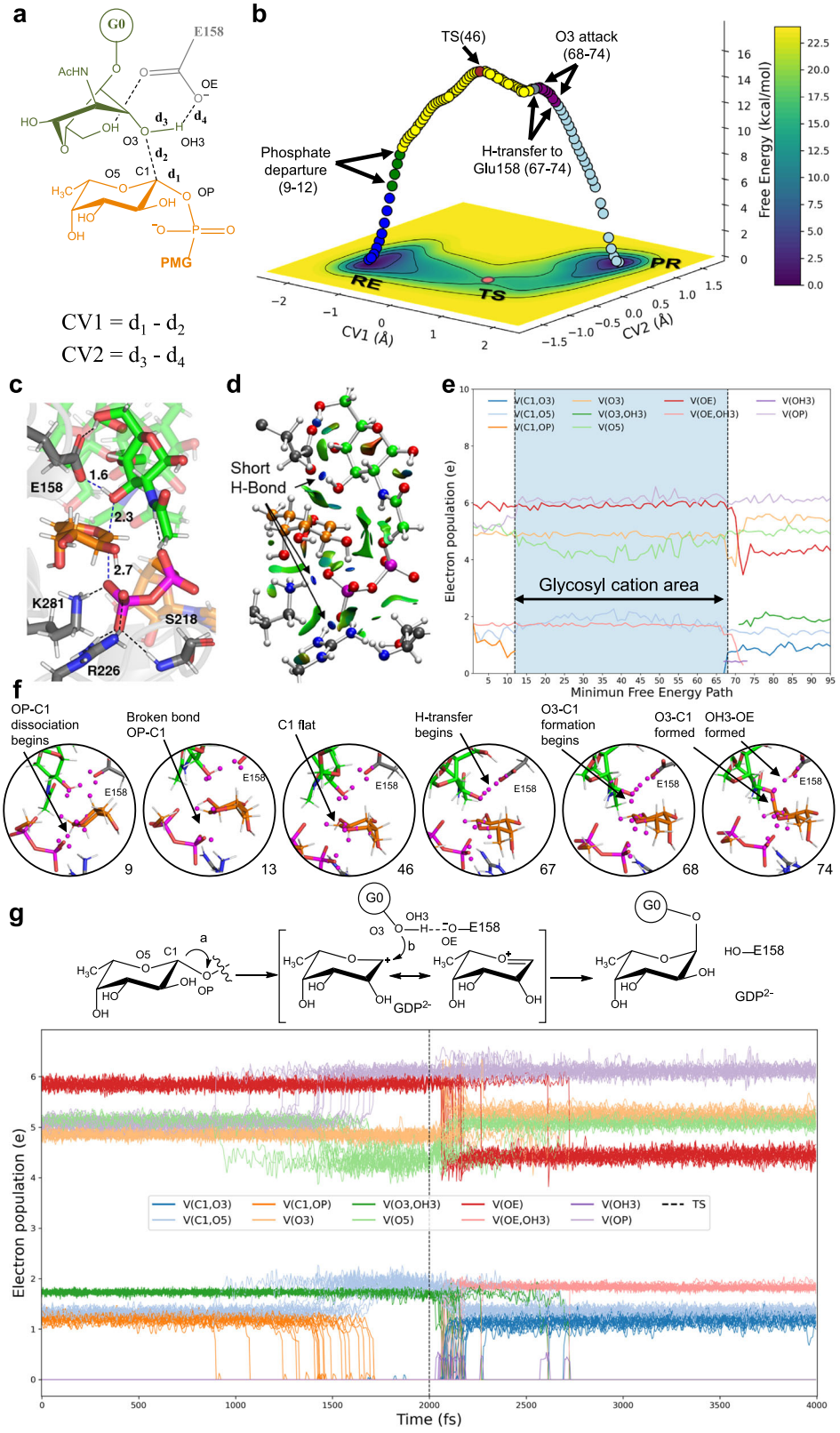

to this analysis, a transient glycosyl cation exists, placing this reaction on the borderline between S_N1 and S_N2 mechanisms.

The ELF analysis along the MFEP reveals the presence of a transient intermediate, but does not provide information about its lifetime. For this, molecular dynamics simulations are required, considering some geometric feature that distinguishes the different reaction stages, as we have previously demonstrated for organocatalytic (non-enzymatic) reactions. In our case, for example, the planarity of C1 could be considered a potential criterion. Unfortunately, the amplitude of C–H bond vibrations makes it difficult to pinpoint the precise moment when C1 becomes planar and when it re-pyramidalizes. Since this is an enzymatic reaction, molecular dynamics simulations tend to be highly reproducible, and generally only a few replicas are sufficient to gain insight into the system's temporal evolution. Nevertheless, due

Fig. 6 | Key electronic and structural events in the fucose transfer reaction catalyzed by AtFUT11. a Schematic representation of the key distances involved in the glycosyl transfer reaction, including the acceptor G0, donor (GDP-Fuc), and catalytic base (Glu158). **b** Free energy surface (FES) projected onto two collective variables (CV1: glycosidic bond formation; CV2: proton transfer). The XY plane shows the positions of the reactant (RE), transition state (TS), and product (PR), while the Z-axis displays representative snapshots along the minimum free-energy pathway (MFEP). Key mechanistic stages are annotated along the MFEP: blue, C1–OP bond intact; green, bond cleavage; yellow, oxocarbenium-like intermediate; brown, transition state; slate gray, onset of proton transfer; purple, nucleophilic attack; magenta, both events underway; light blue, glycosidic bond formed. Source data are provided as a Source data file. **c** Structural model of the TS, showing distances involved in bond cleavage and formation, and key residues stabilizing the TS via electrostatic interactions. H-bonds are showed in black dashed lines and key distances in blue dashed lines. **d** Non-covalent interaction (NCI) analysis of the TS, confirming stabilization via hydrogen bonding and showing that proton transfer has not yet begun. **e** Electron localization function (ELF) analysis along the MFEP, highlighting the sequential nature of bond-breaking and bond-forming events. Source data are provided as a Source data file. **f** Representation of the descriptors (shown as magenta spheres) for the indicated points in the ELF analysis. See Supplementary Movie 2 for the evolution of the descriptors. **g** Top: schematic depiction of the carbocationic intermediate stabilized by resonance. Bottom: ELF analysis of 20 reactive trajectories, confirming the transient yet consistent formation of a glycosyl cation (for per-replicate analyses, see 10.5281/zenodo.17558724). In all panels, *At*FUT11 carbon atoms are shown in grey, the G0 glycan in green, and the GDP-Fuc donor in orange. In ELF analyses only evolution of those basins involved in the reaction are shown. All atom labels correspond to those defined in (**a**). Source data are provided as a Source data file.

to the stochastic nature of these simulations, a certain number of replicas is necessary. Our approach in this work is to perform a series of QM/MM/MD simulations of the reaction, including several replicas, and then apply ELF analysis to the resulting trajectories.

Under these conditions, we obtain plots in which the x-axis corresponding to reaction time, which allows us to estimate, at least approximately, the lifetime range of the glycosyl cation (Fig. 6e). It should be noted that ELF analysis must be performed on all QM/MM/MD simulations, and together with the high computational cost of each QM/MM/MD run, this results in a very demanding overall computational workload, thereby limiting the precision of time estimates.

To obtain reactive trajectories connecting RE and PR through the TS, a total of 20 independent replica pairs were generated from the TS using unbiased QM/MM/MD. For each replica, two runs were performed: one with random Maxwell–Boltzmann initial velocities and another with their opposite values ($v \rightarrow -v$), thus yielding complementary TS → RE and TS → PR connections. Each branch was propagated for 2 ps (4 ps per replica after concatenation into RE → TS → PR trajectories). Trajectories were saved every 5 fs, resulting in 800 frames per concatenated replica. These linked trajectories were used to estimate event lifetimes and verify basin connectivity in collective-variable space (Fig. 6g) (For per-replicate analyses, see 10.5281/zenodo.17558724).

The data shown in Fig. 6e, g clearly reveal a defined temporal window between GDP departure and the formation of the new O3–C1 glycosidic bond, corroborated by the concerted evolution of key reactivity distances (d_1–d_4), a transient shortening of C1–O5, and a reduction in the distance of C1 from the O5–H–C2 plane, together consistent with transient glycosidic oxocarbenium-like character (Supplementary Fig. 13).

Notably, we observe an increased population of the C1–O5 basin, consistent with resonance stabilization of a transient glycosyl cation during this interval. Despite some variability, with gaps extending up to 800 fs, no combination of trajectories yields a lifetime for the carbocation species shorter than 500 fs, supporting the interpretation of a transient state consistent with the existence of a transient intermediate. Consequently, although a classical S_N1 mechanism involving an intimate ion pair and full configuration inversion cannot be definitively confirmed, the data strongly support a pathway that lies at the borderline between S_N2 and S_N1 mechanisms. The process appears to be concerted yet highly asynchronous, with sufficient temporal separation between key chemical events to impart partial intermediate character, while still ensuring inversion of configuration. In essence, FUT11 catalyzes fucose transfer through a mechanism that skirts the edge of S_N1 territory.

*At*FUT11 can synthesize Lewis^x

Finally, a comparison of the *Hs*FUT9 crystal structures complexed with GDP-H-type 2 and GDP-extended type 2 lacto-N-neotetraose (LNnT) with the *At*FUT11-GDP-G0 complex revealed that the chitobiose of G0 aligns well with the GlcNAc and Gal residues of the H-type 2 and LNnT oligosaccharides (Fig. 7a). This structural similarity indicates that *At*FUT11 can also fucosylate type 2 LacNAc substrates, thereby generating the Lewis^x structures. To confirm this, we incubated *At*FUT11 with GDP-Fuc and a Lewis^x precursor, specifically *p*-nitrophenyl N-acetyl lactosamine, revealing that *At*FUT11 is capable of fucosylating this derivative in a modest yield of 7.6% as determined by UHPLC/ESI-TOF-MS analysis. While the activity is weak, it is not unexpected given the structural similarity to *Hs*FUT9 and their shared membership in the GT10 family[58]. This supports the idea that *At*FUT11 retains structural elements common to antenna-fucosylating enzymes, explaining its latent activity on LacNAc. Rather than reflecting an unusual gain-of-function, this side activity illustrates a shared structural and evolutionary origin within GT10, emphasizing the inherent flexibility of this fold. Overall, these findings indicate that the GT10 architecture of *At*FUT11 enables partial functional overlap with mammalian antenna-FUTs such as FUT9. Its ability to generate Lewis^x in vitro—albeit at much lower efficiency than core α1,3-fucosylation of G0 (compare Fig. 7b vs 1a)—represents a suboptimal yet mechanistically plausible activity, highlighting how GT10 structural features support evolutionary plasticity and expanded substrate scope, even in enzymes specialized for core fucosylation.

It is noteworthy that this dual activity (core and LacNAc fucosylation) is not unprecedented; in *C. elegans*, a related enzyme, CEFT1 catalyzes both core α1,3-fucosylation and, to a minor extent, Lewis^x antigen synthesis on distinct acceptor types[59]. By contrast, CEFT2 does not catalyze core fucosylation but instead acts exclusively on LacdiNAc acceptors[59].

However, it is important to note that there is currently no evidence supporting a physiological role for Lewis^x synthesis by *At*FUT11 in Arabidopsis or other plants. Unlike animals, where Lewis^x plays important biological roles[60], these epitopes are not naturally detected in plants[61,62], and the low in vitro activity likely reflects enzymatic promiscuity and structural conservation rather than a biologically significant process. Thus, while the ability of *At*FUT11 to fucosylate Lewis^x precursors in vitro is intriguing as an example of catalytic flexibility, it does not imply direct physiological relevance.

Discussion

This study provides a comprehensive understanding of *At*FUT11, a plant glycosyltransferase that catalyzes the plant core α1,3-fucosylation of N-glycans—a critical post-translational modification. Using an integrated approach combining glycan microarray profiling, crystallography, enzymatic assays, and computational simulations, we elucidated how *At*FUT11 achieves substrate selectivity, catalysis, and molecular adaptability.

The structural analysis revealed a modular GT-B architecture in *At*FUT11, composed of a Rossmann fold donor domain and an acceptor domain formed by interacting N-terminal and Rossmann subdomains. This arrangement enables specific recognition of the α1,3 arm of N-

https://doi.org/10.1038/s41467-026-68786-6

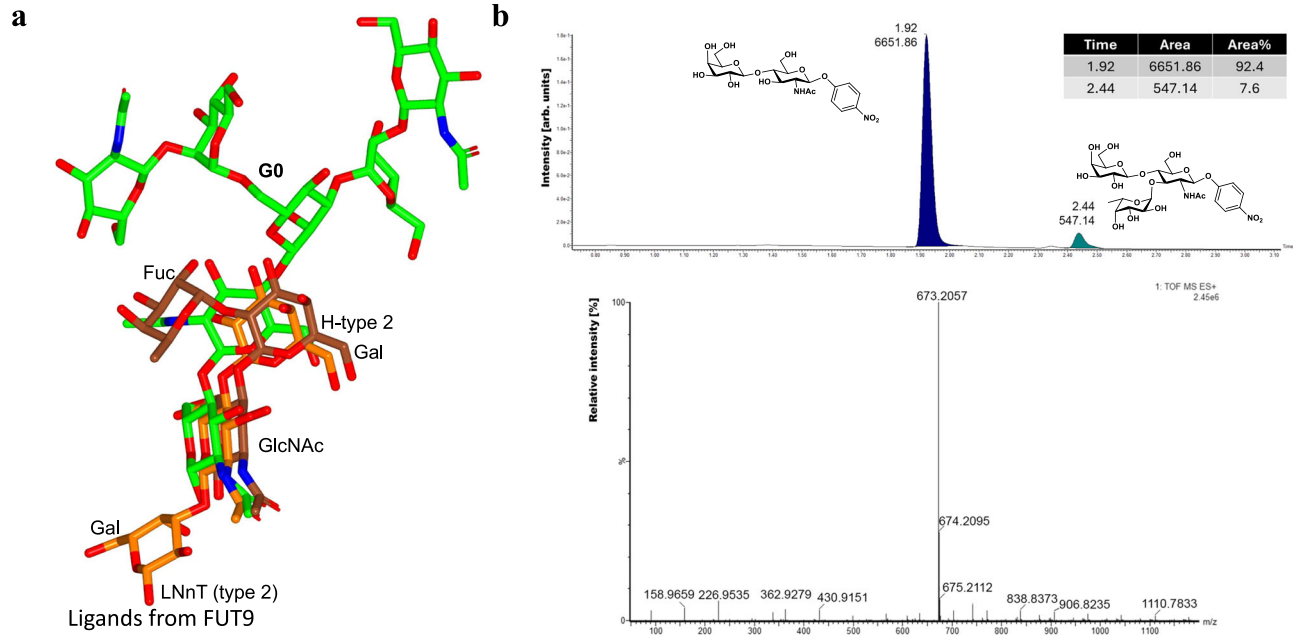

Fig. 7 | AtFUT11 is capable of synthesizing Lewis^x. a Superposition of G0 (green carbon atoms) with oligosaccharides (H-type 2 shown as brown carbon atoms and LNnT as orange carbon atoms) bound to *Hs*FUT9. **b** (upper panel) UHPLC trace showing the formation of Lewis^x derivative (retention time: 2.44 min in 7.6 % conversion) after the incubation of *p*-nitrophenyl N-acetyllactosamine (retention time: 1.92 min) with *At*FUT11 in the presence of GDP-Fuc at room temperature for 18 h. (lower panel) Mass spectrum positive mode corresponding to peak with retention time 2.44 min.

glycans, while accommodating β1,2-xylose and tolerating variability at the α1,6 arm. The syn-ψ conformation adopted by the G0 chitobiose is required for catalysis, as it positions the innermost GlcNAc OH3 for fucosylation. The solvent exposure of the α1,6 arm further underscores *At*FUT11's tolerance at this branch. Substrate specificity is also shaped by its ability to accommodate terminal galactose while excluding GalNAc at the E^{G0} position. Functional assays confirmed weak LacNAc fucosylation by *At*FUT11—a promiscuous activity possibly reflecting structural similarity to mammalian antenna-FUTs. This residual activity broadens *At*FUT11's functional repertoire and suggests evolutionary convergence in glycan recognition.

By comparing the activity of wild-type *At*FUT11 with that of four active site mutants, we identified Glu158, Tyr192, and Glu197 as critical for substrate binding and catalysis. These residues, along with others involved in GDP and G0 recognition, are fully conserved in *At*FUT12, supporting a shared catalytic architecture among *Arabidopsis thaliana* isoforms. *At*FUT11's structural tolerance for modifications, such as fucosylation at A^{G0} OH6 or β1,2-xylose at C^{G0}, reinforces its functional plasticity, positioning it as a versatile tool in plant-based glycoengineering platforms—particularly where compatibility with native plant N-glycans or custom antenna fucosylation is desired. Although core α1,6-fucosylation is exclusive to mammals, *At*FUT11's ability to accept such modified substrates reflects a surprising mechanistic flexibility.

Despite their differing architectures, FUT11, FUT8[9], and MGAT2[39] all rely on additional structural modules to engage N-glycan substrates, highlighting a convergent strategy for achieving substrate specificity through modular recognition. Glycan microarray analyses also reveal that FUT11 and FUT8[9] share remarkably similar substrate preferences: both enzymes require a terminal GlcNAc on the α1,3 arm and accommodate structural variability at the α1,6 arm, including β1,2-xylose. Notably, while FUT11 readily accepts N-glycans already modified with core α1,6-fucose, FUT8 is incompatible with core α1,3-fucosylation due to steric clashes at its acceptor binding site[9].

The most distinctive mechanistic observation uncovered by this study suggests *At*FUT11 may modulate its acceptor substrate's conformation. Glu158 may help promote a transient conformational distortion of the innermost GlcNAc, shifting it from its canonical $^4C_1$ chair to a puckered state. This distortion aligns the acceptor hydroxyl for nucleophilic attack and enables fucosyl transfer via an asynchronous S_N1–S_N2-like mechanism involving a transient glycosyl cation. This may represent a previously underappreciated mode of conformational catalysis in glycosyltransferases—driven not only by donor activation, but also by enzyme-enforced distortion of the acceptor substrate. The carbocation-like species discussed in this work does not correspond to a typical thermodynamic intermediate featuring a local minimum, but to a transient short-lived oxocarbenium-like configuration identified from the topology of the free-energy surface obtained by ab initio metadynamics and defined in relation to a time scale fixed by the metadynamics conditions. While different exchange–correlation functionals may affect the lifetime and energetic profile of this transient species, our conclusions are supported by the consistent observation of this oxocarbenium-like character across a statistically significant ensemble of independent molecular-dynamics trajectories, analyzed using the ELF formalism. None of the trajectories evolves toward either a fully stabilized carbocation minimum or a purely concerted S_N2 pathway, indicating that the reaction consistently lies within an S_N1–S_N2 continuum. These mechanistic insights not only refine our understanding of *At*FUT11 but expand the conceptual repertoire of catalytic strategies used by glycosyltransferases.

In summary, this work supports a model consistent with acceptor-influenced conformational catalysis as an additional mechanistic principle in glycosyltransferase function, fundamentally recasting the acceptor's role from a passive scaffold to an active participant in catalysis. Our findings extend the molecular understanding of plant-specific N-glycosylation and inform the rational engineering of fucosylation pathways across biological kingdoms. By combining structural, biochemical, and computational evidence, we provide a mechanistic blueprint for designing enzymes with tailored substrate specificity and catalytic control, with broad implications for biotechnology and synthetic biology, including the development of glycoprotein-based therapeutics.

Methods

Expression and purification of *At*FUT11

The DNA sequence encoding amino acid residues 84–501 of *At*FUT11 was codon optimized and synthesized by GenScript (USA) for expression in HEK293F cells (Thermo Fisher Scientific, R79007). The DNA, containing at the 5′-end a recognition sequence for *Kpn*I, and at the 3′ end a stop codon and a recognition sequence for *Xho*I, was cloned into a modified pHLSec containing after the secretion signal sequence, a 12xHis tag, a superfolder GFP and a Tobacco Etch Virus (TEV) cleavage site, rendering the vector pHLSec-12Hist-GFP-TEV-*At*FUT11(84–501). Both the synthesis of the *At*FUT11 construct and the engineered pHLSec together with the cloning of *At*FUT11 into pHLSec-12His-*GFP*-TEV were performed by GenScript.

pHLSec-12Hist-GFP-TEV-*At*FUT11(84-end) was transfected into the HEK293F cell line (Thermo Fisher Scientific) as described below. Cells were grown in suspension in a humidified 37 °C and 5% CO_2 incubator with rotation at 130 r.p.m. using F17 serum-free media with 2% Glutamax and 0.1% P188. Transfection was performed at a cell density of 2.5×10^6 cell/mL in fresh media using a ratio of 3 µg plasmid per mL of cell culture. Cells were then incubated 5 min at 37 °C and PEI-MAX 40 K (1 mg/mL) was added to the cell culture flask in a ratio of 9 µg PEI per mL of cell culture. At the time of transfection, Kifunensine-Bio-X (CarboSynth) was added to the culture (5 µM final concentration) to facilitate trimming of N-glycans during the purification.

After 24 h post-transfection, cells were diluted 1:1 with pre-warmed media supplemented with valproic acid to a final concentration of 2.2 mM. Cells were harvested 6 days post-transfection by spinning down at 300 × *g* for 5 min, after which the supernatants were collected and centrifuged at 4000 × *g* for 15 min.

Supernatant was loaded into a HisTrap™ Excel Column (GE Healthcare). Protein was eluted with an imidazole gradient from 10 mM (buffer A: 25 mM TRIS pH 7.5, 500 mM NaCl, 10 mM imidazole) up to 500 mM (buffer B: 25 mM TRIS pH 7.5, 500 mM NaCl, 500 mM Imidazole). Buffer was then exchanged to buffer C (25 mM TRIS pH 7.5, 150 mM NaCl) using a HiPrep 26/10 Desalting Column (GE Healthcare). Thereafter, the TEV recognition site was cleaved using TEV protease, added in a ratio of 1:50 (TEV:protein) to the fusion construct in order to cleavage the His-GFP tag. After 20 h of reaction at 18 °C, the cleavage was satisfactorily verified through SDS-PAGE.

TEV protease and GFP were later removed from the solution using a HisTrap Column (GE Healthcare), and isolated *At*FUT11 was dialyzed to buffer D (25 mM MES pH 6.5, 150 mM NaCl). Endoglycosidase-H (Endo-H) was then added in a ratio 3:250 (Endo-H:protein) in order to trim the N-glycans. After 20 h of reaction at 18 °C, the cleavage was verified through SDS-PAGE. Endo-H was later removed from the solution using a MBP-Trap Column (GE Healthcare), and deglycosylated *At*FUT11 was then loaded into a HiLoad 26/60 Superdex 75 Colum (GE Healthcare), previously equilibrated with buffer C.

The protein was concentrated using Amicon Ultra-15mL (Merck) and quantification of protein was carried out by absorbance at 280 nm using its theoretical extinction coefficient ($\varepsilon_{280\ nm}^{AtFUT11}$ = 46465–45,840 $M^{-1}\,cm^{-1}$).

Reaction of *At*FUT11 with G0 N-glycan

G0 glycopeptide (peptide: NH_2-Lys-Val-Ala-Asn-Lys-Thr-CO_2H) was isolated from chicken egg yolk as previously described[9]. A solution containing G0 glycopeptide (10 nmol) and GDP-Fuc (20 nmol) were incubated in the presence of *At*FUT11 (70 µg) in TBS buffer (Tris 50 mM, 150 mM NaCl, pH = 7.5) at room temperature for 18 h. The reaction mixture was analyzed by MALDI-TOF mass spectrometry, performed on an Ultraflextreme III time-of-flight mass spectrometer equipped with a pulsed N_2 laser (337 nm) and controlled by FlexControl 3.3 software (Bruker Daltonics). 2,5-Dihydroxybenzoic acid (DHB) (5 mg/mL in 70/30 ACN:water with 0.1% TFA) was employed as matrix. Reaction mixture (1 µL) was spotted on MTP 384 polished steel MALDI plate and dried. Matrix (1 µL) was spotted on top, dried and measured (n = 2). G0 glycopeptide was included as control. Data was analyzed employing FlexAnalysis 3.3 software (Bruker Daltonics). Raw mass spectrometry data have been deposited in the GlycoPOST repository under accession GPST000666.

Microarray screening of *At*FUT11 activity

A collection of aminopentyl functionalized glycans (144 structures) were immobilized on NHS activated microarray slides as previously described[9]. After printing, the microarrays were incubated overnight at room temperature with a solution (200 µL) containing recombinant *At*FUT11 (58 µg) with GDP-Fuc (500 µM) in TBS buffer (50 Mm TRIS, 150 mM NaCl, pH = 7.5). After incubation, the microarrays are washed with TBST (50 mM TRIS, 150 mM NaCl, pH = 7.5 + 0.01% Tween 20) and water. Solutions of fluorescently labelled (Alexa Fluor-555) *Aleuria aurantia* lectin (Vector Lab, L-1390-2, 1.4 µM) and Anti-HRP (Merck, P7899, 2.0 µM) in TBST (50 mM TRIS, 150 mM NaCl, pH = 7.5 + 0.01% Tween 20) were incubated in the dark at room temperature for 1 hour. As controls unreacted microarrays were incubated with AAL-555 and anti-HRP-555. After incubation, microarrays were washed with TBST and water, dried in a slide spinner and fluorescence was measured in Agilent G265BA microarray scanner system (Agilent Technologies, Santa Clara, USA). Quantification was performed with ProScanArray® Express (Perkin Elmer, Shelton, USA) and Microsoft Excel. Average of mean relative fluorescence units (RFU) values after local background subtraction and standard deviation for four replicates spots were represented as histograms employing GraphPad Prism 6 software.

Crystallization and data collection

Purified *At*FUT11 was concentrated and co-crystallized with 5 mM GDP and 1.5 mM G0 in the absence of NaCl. Appropriate size of crystals were grown by sitting drop experiments at 18 °C by mixing 0.5 µL of protein solution (5.5 mg/mL *At*FUT11, 5 mM GDP and 1.5 mM G0 in 25 mM TRIS pH 7.5) with an equal volume of a reservoir solution (90 mM LiNaK, 0.1 M TRIS pH 8 and 32.5% precipitant mix 6) (Molecular Dimensions) and 0.25 µL of an additive solution (40% Acetonitrile) (Hampton Research). The crystals were cryoprotected in mother liquor containing 25% glycerol and flash frozen in liquid nitrogen.

Structure determination and refinement

The data were collected in the beamline BL13 XALOC of ALBA at a wavelength of 0.97 Å and a temperature of 100 K. Data were processed and scaled using XDS[63] and CCP4[64] software packages. Relevant statistics are given in Table 1. The crystal structure was solved by molecular replacement with Phaser[64] using a model generated with AlphaFold[65] as the template. Initial phases were further improved by cycles of manual model building in Coot and refinement with REFMAC5[64,66]. Further rounds of Coot and refinement with REFMAC5 were performed to obtain the final structure. The final model was validated with PROCHECK; model statistics are given in Table 1. The Ramachandran plots for the *At*FUT11-GDP-G0 show that 90.3%, 9.7%, 0%, and 0% of the amino acids are in most favoured, allowed, generously allowed and disallowed regions, respectively.

Synthesis of Lewis^x with recombinant *At*FUT11

A solution containing *p*-nitrophenyl N-acetyllactosamine (50 nmol) and GDP-Fuc (100 nmol) were incubated in the presence of *At*FUT11 (288 µg) in TBS buffer (50 mM TRIS, 150 mM NaCl, pH = 7.5) at room temperature for 18 h. The reaction mixture was quenched with acetonitrile and analyzed by ultra-high-performance liquid chromatography and mass spectrometry detection with an electrospray source and high-resolution time-of-flight analyzer (UHPLC/ESI-TOF-MS). The reaction mixture was separated by liquid chromatography using Acquity Premier-type equipment (Waters, Milford, MA, USA) equipped with a BEH HILIC amide type column of dimensions 50 × 2.1 mm and

particle size of 1.7 μm (Waters, Milford, MA, USA). The column temperature was set at 30 °C, and the injection volume was 1 μL. The total analysis time was 20 min. For the chromatographic separation, a mixture of aqueous 100 mM ammonium formiate (A) and ACN (B) as the mobile phases was employed with a gradient as follows: 10% B held for 0.5 min at 0.3 mL min^{-1}, increased linearly to 100% B over 4.5 min at 0.2 mL min^{-1}, held at 100% B for 2 min at 0.2 mL min^{-1}, then returned to 10% B over 0.5 min and equilibrated for 3.5 min at 0.3 mL min^{-1}. The peak mass detection was carried out using ESI-QTOF Synapt XS equipment (Waters, Milford, MA, USA). All instrumental parameters were optimized to obtain the best signal, the capillary voltage and cone voltage were firmly set to 700 and 50 V, respectively, while the nebulization and cone gas flow rates were firmly set at 700 and 150 L/h, respectively, and the nebulization and source temperatures were set at 350 °C. The acquisition was performed in positive mode with the mass range *m/z* 50–1200 Da. Data were processed using MassLynx v4.2 (Waters, Milford, MA, USA). UV detection was set to 298 nm. Peaks were integrated and mass spectra were analysed. The formation of a new peak (t_R= 2.44 min) corresponding to the mass of *p*-nitrophenyl Lewis^x was observed. *m/z* $[M+Na]^+$, calculated for $C_{26}H_{38}N_2NaO_{17}$ 673.2068, found 673.2057. Raw mass spectrometry data have been deposited in the GlycoPOST repository under accession GPST000666.

Cell culture

The original HEK293 was obtained from ATCC (CRL-1573) and used for glycoengineered experiments. All isogenic glycoengineered HEK293 cell lines were cultured in DMEM (Sigma-Aldrich) supplemented with 10% heat-inactivated fetal bovine serum (Sigma-Aldrich) and 2 mM GlutaMAX (Gibco) in a humidified incubator at 37 °C and 5% CO_2.

CRISPR/Cas9-targeted KO in HEK293 cells

CRISPR/Cas9 knockout (KO) was conducted using the GlycoCRISPR resource, which includes validated gRNA libraries targeting all human glycosyltransferases (GTs)[67]. HEK293^{Biantennary} (KO *ST3GAL4/6*, *ST6GAL1*, *FUT4*, *B4GALNT3/4*, and *MGAT3/4A/4B/5*) cells were developed through four rounds of KO: the first targeting *B4GALNT3/4* and *MGAT3*; the second targeting *FUT4*, *ST3GAL4/6*, and *ST6GAL1*; the third targeting *MGAT4A/4B/5*; and the fourth targeting *FUT8*. In each round, HEK293 cells were cultured in 6-well plates until approximately 70% confluence and transfected with a total of 3 μg of gRNA and GFP-tagged Cas9-PBKS plasmid using Lipofectamine 3000 (ThermoFisher Scientific), following the manufacturer's instructions. One day after the transfection, GFP-positive cells were bulk-sorted using FACS (SONY SH800). After a week of culture, bulk-sorted cells were single-cell sorted into 96-well plates. KO clones were screened by Indel Detection via Amplicon Analysis PCR with primers amplifying the gRNA target sites, and indel sequences were further confirmed through Sanger sequencing. All gRNA and primers were synthesized by TAG Copenhagen A/S, and their sequences are listed in Supplementary Table 3.

*At*FUT11 construct design and site-directed mutagenesis

The synthetic full-length DNA of *At3g19280* (also known as *AtFucTA* or *FUT11*) was previously synthesized[20] and cloned into the EPB71 vector (Addgene #90018) using BamHI and NotI restriction sites, enabling targeted integration into the human AAVS1 safe harbor locus. Mutations of four candidate residues (E158, Y192, E197, and H361) to alanine were introduced individually using the PrimeSTAR Mutagenesis Basal Kit (Takara Bio).

ZFN KI of *At*FUT11 variants in HEK293^{Biantennary} cells

For site-directed knock-in (KI), a modified ObLiGaRe approach targeting the AAVS1 safe harbor site was employed, utilizing two inverted ZFN binding sites flanking the *At*FUT11 variants within the donor plasmids. KI was carried out as previously described. Briefly, HEK293^{Biantennary} cells were grown in 6-well plates to ~70% confluency and transfected with 1 μg of each ZFN tagged with GFP or Crimson alongside 2 μg of donor plasmid. 48 h post-transfection, cells expressing both GFP and Crimson were enriched by FACS (Sony SH800), and following one week of culture, the bulk-sorted cells were single-cell sorted into 96-well plates. The targeted KI single clones were screened by junction PCR using primer pairs specific to the junction between the donor plasmid and the human AAVS1 locus. All primers were synthesized by TAG Copenhagen A/S, and their sequences are listed in Supplementary Table 3.

Flow cytometry analysis

The level of α3 fucose structures on the cell surface was measured by flow cytometry using a rabbit polyclonal antibody specific for α3 fucose glycosylation. Cells were washed with PBS containing 1% BSA (PBA) and incubated on ice with α3 Fuc pAb (Agrisera, AS07 268, 1:500 dilution in PBA) or biotinylated LCA lectins (Vector lab, B-1045-5, 0.5 μg/mL in PBA) for 1 h, followed by washing and incubation with Alexa Fluor 647-conjugated goat anti-rabbit IgG (Invitrogen, A21245, 1 μg/mL in PBA) or Alexa Fluor 647-conjugated streptavidin (Invitrogen, S32357, 1 μg/mL in PBA) for 30 min. Cells were then resuspended for flow cytometry analysis (Sony SA3800), and the mean fluorescent intensity (MFI) of α3 Fuc pAb binding was quantified using FlowJo software (FlowJo LLC).

MC model building

The Michaelis complex (MC), comprising the protein, the acceptor hexasaccharide (G0), and GDP-fucose (GDP-Fuc), was generated based on the crystal structure of the ternary complex (*At*FUT11, G0 and GDP). The GDP-Fuc coordinates were obtained by superimposing the nucleoside moiety of GDP-Fuc (from *Hp*FUT complexed with GDP-Fuc PDB: 2NZY) onto the GDP molecule in the experimental structure, yielding the ternary model used for molecular dynamics (MD) simulations. All additional models used in this study were derived from this initial configuration. In the case of the E158A mutant, the substitution was performed using the mutagenesis tool implemented in PyMOL[68] Protonation states were assigned using PROPKA3[69] at pH ≈ 7.0 for all models. All trajectory analyses were performed with CPTRAJ software[70] as implemented in AMBER23[71]. Root-mean-square deviation (RMSD) analyses were carried out using the first snapshot following the second equilibration step as reference (see below).

Molecular dynamics simulations

All molecular dynamics (MD) simulations were performed using the AMBER23 simulation package[71]. The protein was modeled using the FF14SB force field[72], while the acceptor glycan (G0) was described using the GLYCAM06 force field[73]. The donor substrate GDP-Fuc was parametrized using the ANTECHAMBER module within AmberTools23, employing GAFF as the base force field and AM1-BCC for partial atomic charge calculation[74,75]. Michaelis complex (MC) was constructed using the LEaP module in AmberTools23[76]. The system was solvated in a 15 Å orthorhombic TIP3P water box[77,78] (box dimensions 117.2 × 79.4 × 92.2 $Å^3$), and electroneutrality was achieved by adding two Cl^- counterions, resulting in a total of 21,507 water molecules.

A standardized five-step equilibration protocol was applied:

(i) Solvent minimization: 5000 steps, including 2500 steepest descent followed by 2500 conjugate gradient steps, with harmonic restraints on the solute (protein and ligands). (ii) Unrestrained minimization: An additional 5000 steps under the same conditions without restraints. (iii) Gradual heating: The system was heated from 0 K to 300 K under constant pressure (1 atm) using periodic boundary conditions. Harmonic restraints of 30 kcal/mol were applied to the solute. Langevin dynamics were used for temperature control[79] with a 1 fs timestep. Long-range electrostatics were handled using the Ple Mesh Ewald method[80] and a non-bonded cutoff of 8 Å was applied for

Lennard-Jones interactions. (iv) Equilibration: The system was equilibrated for 2 ns under NVT conditions at 300 K using a 2 fs timestep. This step was repeated to confirm system stability. (v) Production runs: Final MD simulations were performed under constant volume and temperature (300 K), using a Langevin thermostat with a collision frequency of 2.0 ps^{-1}. All bonds involving hydrogen atoms were constrained using the SHAKE algorithm[81] with a 2 fs timestep for integration.

QM/MM molecular dynamics simulations

QM/MM molecular dynamics simulations were carried out using the CP2K (version 2022.1) simulation package[82], in combination with PLUMED2[83] for trajectory monitoring and collective variable tracking. Simulation models were prepared by extracting representative snapshots from preceding classical MD simulations.

The quantum region comprised 49 atoms enclosed within an orthorhombic box of 16.5960 × 17.2951 × 13.7381 Å³. This QM region included the innermost N-acetylglucosamine (GlcNAc), atoms C1, C2, O5, and C5 of the adjacent sugar ring, and their respective substituents. QM–MM boundaries were saturated with hydrogen link atoms (see Supplementary Fig. 14). QM atoms were treated using the semi-empirical PM6 method, selected to capture the conformational behavior of the A^{G0} unit while maintaining computational efficiency. The MM atoms were described using the same force fields employed in the classical MD simulations. The MM environment consisted of a periodic orthorhombic box (74.9 × 122.8 × 90.2 Å³) containing 21,508 TIP3P water molecules and 2 Cl^- counterions.

All QM/MM/MD simulations followed a standardized multi-step protocol: (i) a progressive annealing phase to relieve steric clashes, (ii) a 5 ps QM/MM equilibration run in the NVT ensemble at 300 K with a timestep of 0.5 fs and no external bias, allowing the system to relax at the QM/MM level, (iii) a 100 ps production simulation at 300 K under NVT conditions, with a 1 fs integration timestep. Five independent replicas were performed for each model, restarting the velocity distribution in each run to enhance sampling of the conformational landscape of the enzyme–substrate complex[84].

QM/MM/MD metadynamics simulations

Metadynamics simulations were performed using CP2K[82] in combination with the metadynamics algorithm implemented in PLUMED 2[83] which was also used to monitor collective variables (Supplementary Fig. 15) and compute the associated FES. Starting structures were derived from the MC described above. The MM region was treated using the same force fields as in the classical MD simulations, while the QM region (see Supplementary Fig. 14) was described using density functional theory (DFT) with the PBE exchange–correlation functional[85]. This choice is consistent with previous studies on glycosyltransferases[43] and carbohydrate conformational analysis[86].

The QM region was treated using the Gaussian and plane waves (GPW) approach. The electronic wavefunctions were expanded with the triple-ζ valence polarized TZV2P basis set[87], and the electron density was converged using an auxiliary plane-wave basis set with a variable cutoff, optimized for each model. GTH pseudopotentials were used to describe core electrons[88].

All metadynamics simulations followed a standardized protocol: (i) optimization of the plane-wave density cutoff for each system, (ii) a multi-step annealing process to remove residual strain, (iii) a 5 ps QM/MM equilibration run at 300 K under NVT conditions with a 0.5 fs timestep and no external bias, (iv) the production metadynamics simulation, initiated from the final snapshot of the equilibration phase.

In specific simulations, distance restraints were applied. These were implemented using the uwalls module in PLUMED2[83].

Free energy landscapes of carbohydrate units

The conformational free energy landscape (FEL) of the innermost GlcNAc subunit of the G0 acceptor and the fucose moiety from GDP-Fuc was computed for different models using collective variables derived from Cremer–Pople puckering[89]. coordinates. Specifically, Cartesian projection coordinates normalized by the puckering amplitude (Q) were employed:

$$CV1 = \frac{q_x}{Q} \tag{3}$$

$$CV2 = \frac{q_y}{Q} \tag{4}$$

$$CV3 = \frac{q_z}{Q} \tag{5}$$

In all cases, the reweighting of the puckering coordinates θ and ϕ was performed using PLUMED2[83].

The QM region consisted of the indicated number of atoms enclosed within an orthorhombic box of $a \times b \times c$ Å³. Hydrogen atoms were added to cap the QM–MM boundaries (see Supplementary Fig. 14). Gaussian bias potentials were deposited every 60 fs with an initial height of 1.2 kcal/mol. The widths were set to 0.035, 0.030, and 0.020 collective variable units (c.v.u.) for CV1, CV2, and CV3, respectively. The simulation was extended until the free energy landscape (FEL) reached convergence.

Free energy landscapes of carbohydrates

A detailed summary of the QM/MM system setup, simulation parameters, and convergence times for all carbohydrate free energy landscape calculations is provided in Table 2.

Fucose: The region included the entire fucose moiety, the diphosphate group, and the CH_2 bridge linking the ribose ring to the diphosphate; the metadynamics free-energy reconstruction was terminated upon convergence at 225 ps (7500 deposited Gaussians).

A^{G0}: The region comprised the innermost GlcNAc, along with atoms C1, C2, O5, and C5 of the adjacent sugar and their corresponding substituents.

Table 2 | QM/MM metadynamics parameters for carbohydrate free energy landscape calculations

Carbo-hydrate	NA	QM box ($a \times b \times c$) Å³	t (ps)	Cutoff (Ry)	pbc box ($a' \times b' \times c'$) Å³	WATs	Counter-ions (Cl-)
Fucose	33	14.57 × 15.05 × 13.15	225	250	75.5 × 123.0 × 92.5	21,508	2
A^{G0a}	49	14.99 × 15.83 × 15.84	350	250	74.9 × 122.8 × 90.2	20,551	2
A^{G0b}	49	16.60 × 17.30 × 13.74	350	250	74.9 × 122.8 × 90.2	21,508	2
A^{G0c}	49	16.60 × 17.29 × 13.73	300	270	75.5 × 119.5 × 92.5	20,896	1
A^{G0d}	49	16.58 × 17.29 × 13.75	225	250	75.5 × 124.4 × 92.5	21,775	4
A^{G0e}	49	17.99 × 15.89 × 14.46	350	300	71.3 × 117.5 × 87.4	21,771	3

[a]with restrictions for OH3 activation. [b]in Michaelis Complex. [c]in *At*FUT11-G0-GDP trimer. [d]in *At*FUT11-G0 dimer. [e]in E158A mutant complex. t (ps): time necessary for reaching convergence. NA: number of atoms in the QM region. QM box ($a \times b \times c$): non-periodic orthorhombic QM cell dimensions. pbc box ($a' \times b' \times c'$): periodic MM simulation box used for solvation (Å). WATs: number of water molecules in the MM box. Counter-ions (Cl^-): number of chloride ions added to neutralize the system.

- *With restraints in OH3*, the bias height was reduced to 0.6 kcal/mol after 300 ps (10,000 deposited Gaussians) to enhance sampling accuracy, and the simulation was extended by 50 ps with the lower bias (≈1667 additional Gaussians).
- *In Michaelis complex*, the bias height was reduced to 0.6 kcal/mol after 300 ps (10,000 deposited Gaussians) to enhance sampling accuracy, and the simulation was extended by 50 ps with the lower bias (≈1667 additional Gaussians).
- *In the AtFUT11-GO-GDP complex*, the metadynamics free-energy reconstruction was terminated upon convergence at 300 ps (10,000 deposited Gaussians).
- *In the AtFUT11-GO complex*, the metadynamics free-energy reconstruction was terminated upon convergence at 225 ps (7500 deposited Gaussians).
- *In the E158A mutant complex*, the bias height was reduced to 0.6 kcal/mol after 300 ps (-10,000 deposited Gaussians) to enhance sampling accuracy, and the simulation was extended by 50 ps with the lower bias (≈1667 additional Gaussians).

Activation of the OH3 Group via Interaction with Glu158

The initial structure was a representative snapshot from one of the minima identified in the conformational free energy landscape of the innermost GlcNAc unit (A^{G0b}). The atoms included in the QM region correspond to those previously defined in the conformational free energy landscape studies of the same GlcNAc unit. Hydrogen atoms were added at the QM–MM boundaries for capping purposes. A plane-wave cutoff of 250 Ry was employed. Gaussian bias potentials were deposited every 100 MD steps. To improve precision, an initial bias height of 0.2 kcal/mol and a width of 0.2 were used. To restrict sampling to the subspace directly related to OH3 activation, we applied soft restraining walls (PLUMED uwalls).

The simulation was stopped once the free energy surface reached convergence, which occurred following a switch in the interaction pattern of the OH3 group. A total of 800 Gaussian functions were deposited, with a final simulation time of 40 ps. The MM environment consisted of a periodic orthorhombic box (75.5 × 123.0 × 92.5 Å^3) containing 21,508 TIP3P water molecules and 2 Cl^- counterions.

Fucose transfer free energy surface

Simulations were initiated from a representative snapshot corresponding to the minimum identified in the A^{G0a} puckering analysis, where the OH3 group interacts with the catalytic base. The study of the fucose transfer reaction was performed using a combination of two collective variables (CVs), both defined as differences between key interatomic distances.

CV1 describes the glycosyl transfer process and is defined as the difference between the distance from the anomeric carbon of fucose (C1) to the phosphate oxygen and the distance from C1 to the oxygen at position O3 (OH3 group) of the A subunit of G0, which acts as the nucleophile:

$$CV1 = d_{(C1-OP)} - d_{(C1-O3)} \quad (6)$$

To restrict sampling to the subspace directly related to fucose transfer, we applied soft restraining walls (PLUMED uwalls), thus preventing deviations from the catalytic pose without imposing any bias along CV1 or CV2.

CV2 captures the proton transfer and is calculated as the difference between the distance from O3 to its bonded proton (OH3) and the distance between that same proton and the carboxylate oxygen of Glu158:

$$CV2 = d_{(O3-OH3)} - d_{(OH3-COO^-_{E158})} \quad (7)$$

The QM region included 115 atoms within an orthorhombic box of 21.3830 × 22.2040 × 21.7931 Å^3. This region comprised the side chains of Arg226 and Lys281, the side chain of Glu158 (the catalytic base), the same GDP-Fuc atoms used in the conformational study of fucose, and the atoms from the G0 acceptor subunit included in the previous conformational analyses, excluding C2 and its substituents to reduce computational cost. The QM–MM boundaries were capped with hydrogen atoms (see Supplementary Fig. 14). The MM environment consisted of a periodic orthorhombic box (75.5 × 123.0 × 92.5 Å^3) containing 21,508 TIP3P water molecules and 2 Cl^- counterions.

A plane-wave cutoff of 370 Ry was used. Gaussian bias potentials were deposited every 100 MD steps, with an initial height of 1.0 kcal/mol and a width of 0.2 (c.v.u.) for both CVs. To improve accuracy near the transition state (TS), the bias height was reduced to 0.1 kcal/mol. Following established recommendations[90] the simulation was stopped after observing TS recrossing (Supplementary Fig. 15), yielding a total of 1280 deposited Gaussians over 64 ps. The free energy surface (FES) associated with the fucose transfer was reconstructed from the HILLS file generated during the metadynamics run, using the sum_hills utility in PLUMED2[83]. The resulting surface was further analyzed using the MEPSAnd tool for topological characterization[91], enabling precise identification of the CV coordinates corresponding to the key points along the reaction coordinate. The minimum free-energy path (MFEP), connecting the reactant (RE) and product (PR) states via the TS, was defined as the trajectory following the lowest free energy in the CV1–CV2 space. Evolution of key distances and puckerings along the MFEP is given in Supplementary Figs. 16 and 17.

Representative structures along the MFEP were extracted from the full metadynamics trajectory using the CV coordinates as references. The transition state was confirmed by performing unbiased QM/MM molecular dynamics simulations starting from the TS structure and observing the relaxation of trajectories toward both the RE and PR.

Non-covalent interactions (NCI)

NCI (non-covalent interactions) were computed using the methodology previously described[47]. Semi-quantitative data were obtained with the NCIPLOT4 program[48]. A density cutoff of ρ = 0.5 a.u. was applied and isosurfaces of s(r) = 0.32 were colored by sign(λ2)ρ in the [−0.03,0.03] a.u. range using VMD1.9 software[92].

Electron localization function (ELF)

We used the gradient field of electron localization function (ELF) developed by Silvi and Savin[49,50]. The density.cube and elf.cube files were generated using the module implemented in CP2K (E_DENSITY_CUBE and ELF_CUBE). The obtained cube files for each point were processed with the Multiwfn3.8 software[93,94] to obtain the corresponding information on basins, attractors and population.

RE → TS → PR trajectories

To generate linking trajectories, we ran 20 independent unbiased QM/MM/MD simulations initiated from the TS structure, at the DFT level (PBE/GPW, TZV2P basis, GTH pseudopotentials). Each replica was propagated in the NVT ensemble at 300 K (timestep 0.5 fs). Initial velocities were sampled from a Maxwell–Boltzmann distribution; to ensure independence and reproducibility, distinct random seeds were provided via &GLOBAL SEED in CP2K. For every replica, we launched two runs: one with the assigned velocities and a second with velocity inversion (v → −v), yielding paired TS → RE and TS → PR connections. Each individual trajectory was run for 2 ps, and the paired paths were concatenated to construct a global RE → TS → PR trajectory of 4 ps. These trajectories were then used to estimate event lifetimes.

Kinetic analysis

Enzyme kinetics for *At*FUT11 were determined using the GDP-Glo luminescence assay (Promega). *At*FUT11 was tested in reactions

containing 100 nM enzyme in 25 mM Tris pH 7.5, 150 mM NaCl. To determine the K_m for GDP-Fuc, the reaction contained 500 µM G0 acceptor and GDP-Fuc (2.5–500 µM). To measure the K_m for G0, the reaction contained 500 µM GDP-Fuc and G0 (5 µM–1 mM). Reactions were incubated 30 min at 37 °C, then mixed 1:1 with GDP-detection reagent (5 µL per well) in a white, opaque 384-well plate and incubated in the dark for 1 h at room temperature before measuring with a CLARIOstar (BMG Labtech). To estimate GDP produced, a GDP standard curve was used; values were background-corrected for GDP-Fuc hydrolysis. Data were fit to a nonlinear Michaelis–Menten model in GraphPad Prism 6, from which K_m, k_{cat}, and V_{max} with standard errors were obtained. All experiments were performed in duplicate ($n = 2$), following Promega's recommendations.

Reporting summary

Further information on research design is available in the Nature Portfolio Reporting Summary linked to this article.

Data availability

The crystal structure of the *At*FUT11-GDP-G0 complex was deposited at the RCSB PDB with accession code, 9S6A. Previously published PDB structures used in this study are available under the accession codes: 7YRO, 8D0Q, 8D0W, 8D0U, 8D0P, 8D0R, 2NZX, 2NZY, and 2NZW. Raw mass spectrometry data have been deposited in the GlycoPOST repository under accession GPST000666. The raw data for the simulations can be found in https://doi.org/10.5281/zenodo.17558724. Source data are provided as a Source data file. Source data are provided with this paper.

References

1. Mohanty, S., Chaudhary, B. P. & Zoetewey, D. Structural insight into the mechanism of N-linked glycosylation by oligosaccharyltransferase. *Biomolecules* **10**, 624 (2020).
2. Schjoldager, K. T., Narimatsu, Y., Joshi, H. J. & Clausen, H. Global view of human protein glycosylation pathways and functions. *Nat. Rev. Mol. Cell Biol.* **21**, 729–749 (2020).
3. Nothaft, H. & Szymanski, C. M. Bacterial protein N-glycosylation: new perspectives and applications. *J. Biol. Chem.* **288**, 6912–6920 (2013).
4. Bai, L. & Li, H. Cryo-EM is uncovering the mechanism of eukaryotic protein N-glycosylation. *FEBS J.* **286**, 1638–1644 (2019).
5. Dutta, D., Mandal, C. & Mandal, C. Unusual glycosylation of proteins: beyond the universal sequon and other amino acids. *Biochim. Biophys. Acta Gen. Subj.* **1861**, 3096–3108 (2017).
6. Dell, A., Galadari, A., Sastre, F. & Hitchen, P. Similarities and differences in the glycosylation mechanisms in prokaryotes and eukaryotes. *Int. J. Microbiol.* **2010**, 148178 (2010).
7. Wang, P. et al. Evolution of protein N-glycosylation process in Golgi apparatus which shapes diversity of protein N-glycan structures in plants, animals and fungi. *Sci. Rep.* **7**, 40301 (2017).
8. Strasser, R. Recent developments in deciphering the biological role of plant complex N-glycans. *Front Plant Sci.* **13**, 897549 (2022).
9. Garcia-Garcia, A. et al. Structural basis for substrate specificity and catalysis of alpha1,6-fucosyltransferase. *Nat. Commun.* **11**, 973 (2020).
10. Pan, Q. & Zhang, X. L. Roles of core fucosylation modification in immune system and diseases. *Cell Insight* **4**, 100211 (2025).
11. Both, P. et al. Distantly related plant and nematode core alpha1,3-fucosyltransferases display similar trends in structure-function relationships. *Glycobiology* **21**, 1401–1415 (2011).
12. Takano, S. et al. The rice RCN11 gene encodes beta1,2-xylosyltransferase and is required for plant responses to abiotic stresses and phytohormones. *Plant Sci.* **236**, 75–88 (2015).
13. Strasser, R. Plant protein glycosylation. *Glycobiology* **26**, 926–939 (2016).
14. Wilson, I. B. Glycosylation of proteins in plants and invertebrates. *Curr. Opin. Struct. Biol.* **12**, 569–577 (2002).
15. Harmoko, R. et al. N-glycan containing a core alpha1,3-fucose residue is required for basipetal auxin transport and gravitropic response in rice (Oryza sativa). *N. Phytol.* **212**, 108–122 (2016).
16. Pedersen, C. T. et al. N-glycan maturation mutants in Lotus japonicus for basic and applied glycoprotein research. *Plant J.* **91**, 394–407 (2017).
17. Jung, J. W. et al. Inactivation of the beta (1, 2)-xylosyltransferase and the alpha (1, 3)-fucosyltransferase gene in rice (Oryza sativa) by multiplex CRISPR/Cas9 strategy. *Plant Cell Rep.* **40**, 1025–1035 (2021).
18. Strasser, R., Altmann, F., Mach, L., Glossl, J. & Steinkellner, H. Generation of Arabidopsis thaliana plants with complex N-glycans lacking beta1,2-linked xylose and core alpha1,3-linked fucose. *FEBS Lett.* **561**, 132–136 (2004).
19. Wilson, I. B. et al. Cloning and expression of cDNAs encoding alpha1,3-fucosyltransferase homologues from Arabidopsis thaliana. *Biochim. Biophys. Acta* **1527**, 88–96 (2001).
20. Larsen, J. S. et al. Engineering mammalian cells to produce plant-specific N-glycosylation on proteins. *Glycobiology* **30**, 528–538 (2020).
21. Serna, S., Yan, S., Martin-Lomas, M., Wilson, I. B. & Reichardt, N. C. Fucosyltransferases as synthetic tools: glycan array based substrate selection and core fucosylation of synthetic N-glycans. *J. Am. Chem. Soc.* **133**, 16495–16502 (2011).
22. Bohe, L. & Crich, D. A propos of glycosyl cations and the mechanism of chemical glycosylation; the current state of the art. *Carbohydr. Res.* **403**, 48–59 (2015).
23. Adero, P. O., Amarasekara, H., Wen, P., Bohe, L. & Crich, D. The experimental evidence in support of glycosylation mechanisms at the S(N)1-S(N)2 interface. *Chem. Rev.* **118**, 8242–8284 (2018).
24. Phan, T. B., Nolte, C., Kobayashi, S., Ofial, A. R. & Mayr, H. Can one predict changes from S(N)1 to S(N)2 mechanisms? *J. Am. Chem. Soc.* **131**, 11392–11401 (2009).
25. Santana, A. G. et al. Dissecting the essential role of anomeric beta-triflates in glycosylation reactions. *J. Am. Chem. Soc.* **142**, 12501–12514 (2020).
26. Merino, P. et al. Computational evidence of glycosyl cations. *Org. Biomol. Chem.* **19**, 2350–2365 (2021).
27. Fu, Y., Bernasconi, L. & Liu, P. Ab initio molecular dynamics simulations of the S(N)1/S(N)2 mechanistic continuum in glycosylation reactions. *J. Am. Chem. Soc.* **143**, 1577–1589 (2021).
28. Franconetti, A. et al. Glycosyl oxocarbenium ions: structure, conformation, reactivity, and interactions. *Acc. Chem. Res.* **54**, 2552–2564 (2021).
29. Rini, J. M., Moremen, K. W., Davis, B. G. & Esko, J. D. Glycosyltransferases and Glycan-Processing Enzymes. In *Essentials of Glycobiology*. 4th ed. (Varki, A. et al. Eds) 67–78 (Cold Spring Harbor Laboratory Press, NY, 2022) https://doi.org/10.1101/glycobiology.4e.6.
30. Ardevol, A. & Rovira, C. Reaction mechanisms in carbohydrate-active enzymes: glycoside hydrolases and glycosyltransferases. insights from ab initio quantum mechanics/molecular mechanics dynamic simulations. *J. Am. Chem. Soc.* **137**, 7528–7547 (2015).
31. Garcia-Garcia, A. et al. FUT8-directed core fucosylation of N-glycans is regulated by the glycan structure and protein environment. *ACS Catal.* **11**, 9052–9065 (2021).
32. Echeverria, B. et al. Chemoenzymatic synthesis of N-glycan positional isomers and evidence for branch selective binding by monoclonal antibodies and human C-type lectin receptors. *ACS Chem. Biol.* **13**, 2269–2279 (2018).
33. Paschinger, K., Rendic, D., Lochnit, G., Jantsch, V. & Wilson, I. B. Molecular basis of anti-horseradish peroxidase staining in Caenorhabditis elegans. *J. Biol. Chem.* **279**, 49588–49598 (2004).

34. Holm, L. Dali server: structural unification of protein families. *Nucleic Acids Res.* **50**, W210–W215 (2022).
35. Okada, T., Teramoto, T., Ihara, H., Ikeda, Y. & Kakuta, Y. Crystal structure of mango alpha1,3/alpha1,4-fucosyltransferase elucidates unique elements that regulate Lewis A-dominant oligosaccharide assembly. *Glycobiology* **34**, cwae015 (2024).
36. Kadirvelraj, R. et al. Structural basis for Lewis antigen synthesis by the alpha1,3-fucosyltransferase FUT9. *Nat. Chem. Biol.* **19**, 1022–1030 (2023).
37. Sun, H. Y. et al. Structure and mechanism of Helicobacter pylori fucosyltransferase. A basis for lipopolysaccharide variation and inhibitor design. *J. Biol. Chem.* **282**, 9973–9982 (2007).
38. Corzana, F. et al. The pattern of distribution of amino groups modulates the structure and dynamics of natural aminoglycosides: implications for RNA recognition. *J. Am. Chem. Soc.* **129**, 2849–2865 (2007).
39. Kadirvelraj, R. et al. Human N-acetylglucosaminyltransferase II substrate recognition uses a modular architecture that includes a convergent exosite. *Proc. Natl. Acad. Sci. USA* **115**, 4637–4642 (2018).
40. Moremen, K. W. & Haltiwanger, R. S. Emerging structural insights into glycosyltransferase-mediated synthesis of glycans. *Nat. Chem. Biol.* **15**, 853–864 (2019).
41. Foley, B. L., Tessier, M. B. & Woods, R. J. Carbohydrate force fields. *WIREs Comput. Mol. Sci.* **2**, 652–697 (2012).
42. Bolhuis, P. G., Chandler, D., Dellago, C. & Geissler, P. L. TRANSITION PATH SAMPLING: throwing ropes over rough mountain passes, in the dark. *Annu. Rev. Phys. Chem.* **53**, 291–318 (2002).
43. Piniello, B. et al. Asparagine tautomerization in glycosyltransferase catalysis. The molecular mechanism of protein O-fucosyltransferase 1. *ACS Catal.* **11**, 9926–9932 (2021).
44. Sanz-Martínez, I., García-García, A., Tejero, T., Hurtado-Guerrero, R. & Merino, P. The essential role of waters in the reaction mechanism of protein O-fucosyl transferase 2. *Angew. Chem. Int. Ed.* **61**, e202213610 (2022).
45. Joo, H., Kraka, E., Quapp, W. & Cremer, D. The mechanism of a barrierless reaction: hidden transition state and hidden intermediates in the reaction of methylene with ethene. *Mol. Phys.* **105**, 2697–2717 (2010).
46. Gara, G. et al. Organocatalytic enantioselective vinylcyclopropane-cyclopentene (VCP-CP) rearrangement. *Angew. Chem. Int. Ed.* **62**, e202302416 (2023).
47. Johnson, E. R. et al. Revealing noncovalent interactions. *J. Am. Chem. Soc.* **132**, 6498–6506 (2010).
48. Boto, R. A. et al. NCIPLOT4: fast, robust, and quantitative analysis of noncovalent interactions. *J. Chem. Theory Comput.* **16**, 4150–4158 (2020).
49. Grin, Y., Savin, A. & Silvi, B. In *The Chemical Bond: Fundamental Aspects of Chemical Bonding* (eds. Frenking, G. & Shaik, S.) 345–382 (Wiley-VCH, 2014).
50. Savin, A., Nesper, R., Wengert, S. & Fässler, T. F. ELF: the electron localization function. *Angew. Chem. Int. Ed.* **36**, 1808–1832 (1997).
51. Ortega, A. et al. Catalytic enantioselective Cloke–Wilson rearrangement. *Angew. Chem. Int. Ed.* **57**, 8225–8229 (2018).
52. Capel, E. et al. Absence of intermediates in the BINOL-derived Mg(II)/phosphate-catalyzed desymmetrizative ring expansion of 1-vinylcyclobutanols. *J. Org. Chem.* **87**, 693–707 (2022).
53. Santana, A. G. et al. Dissecting the essential role of anomeric β-triflates in glycosylation reactions. *J. Am. Chem. Soc.* **142**, 12501–12514 (2020).
54. Fang, D., Chaudret, R., Piquemal, J. P. & Cisneros, G. A. Toward a deeper understanding of enzyme reactions using the coupled ELF/NCI analysis: application to DNA repair enzymes. *J. Chem. Theory Comput.* **9**, 2156–2160 (2013).
55. Hix, M. A., Leddin, E. M. & Cisneros, G. A. Combining evolutionary conservation and quantum topological analyses to determine quantum mechanics subsystems for biomolecular quantum mechanics/molecular mechanics simulations. *J. Chem. Theory Comput.* **17**, 4524–4537 (2021).
56. Maghsoud, Y., Dong, C. & Cisneros, G. A. Computational characterization of the inhibition mechanism of xanthine oxidoreductase by topiroxostat. *ACS Catal.* **13**, 6023–6043 (2023).
57. Berger, M. B. & Cisneros, G. A. Distal mutations in the β-clamp of DNA polymerase III* disrupt DNA orientation and affect exonuclease activity. *J. Am. Chem. Soc.* **145**, 3478–3490 (2023).
58. Drula, E. et al. The carbohydrate-active enzyme database: functions and literature. *Nucleic Acids Res.* **50**, D571–D577 (2022).
59. Nguyen, K., van Die, I., Grundahl, K. M., Kawar, Z. S. & Cummings, R. D. Molecular cloning and characterization of the Caenorhabditis elegans alpha1,3-fucosyltransferase family. *Glycobiology* **17**, 586–599 (2007).
60. Schneider, M., Al-Shareffi, E. & Haltiwanger, R. S. Biological functions of fucose in mammals. *Glycobiology* **27**, 601–618 (2017).
61. Strasser, R. Biological significance of complex N-glycans in plants and their impact on plant physiology. *Front Plant Sci.* **5**, 363 (2014).
62. Beihammer, G., Maresch, D., Altmann, F., Van Damme, E. J. M. & Strasser, R. Lewis A glycans are present on proteins involved in cell wall biosynthesis and appear evolutionarily conserved among natural Arabidopsis thaliana accessions. *Front Plant Sci.* **12**, 630891 (2021).
63. Kabsch, W. Xds. *Acta Crystallogr D. Biol. Crystallogr* **66**, 125–132 (2010).
64. Winn, M. D. et al. Overview of the CCP4 suite and current developments. *Acta Crystallogr D. Biol. Crystallogr* **67**, 235–242 (2011).
65. Jumper, J. et al. Highly accurate protein structure prediction with AlphaFold. *Nature* **596**, 583–589 (2021).
66. Murshudov, G. N. et al. REFMAC5 for the refinement of macromolecular crystal structures. *Acta Crystallogr D. Biol. Crystallogr* **67**, 355–367 (2011).
67. Steentoft, C. et al. A validated collection of mouse monoclonal antibodies to human glycosyltransferases functioning in mucin-type O-glycosylation. *Glycobiology* **29**, 645–656 (2019).
68. Schrodinger. *The PyMOL Molecular Graphics System,* Version 3.0. (2024).
69. Olsson, M. H. M., Søndergaard, C. R., Rostkowski, M. & Jensen, J. H. PROPKA3: consistent treatment of internal and surface residues in empirical pKa predictions. *J. Chem. Theory Comput.* **7**, 525–537 (2011).
70. Roe, D. R. & Cheatham, T. E. PTRAJ and CPPTRAJ: software for processing and analysis of molecular dynamics trajectory data. *J. Chem. Theory Comput.* **9**, 3084–3095 (2013).
71. Case, D. A. et al. *AMBER 2023, University of California, San Francisco* (2023).
72. Maier, J. A. et al. ff14SB: improving the accuracy of protein side chain and backbone parameters from ff99SB. *J. Chem. Theory Comput.* **11**, 3696–3713 (2015).
73. Kirschner, K. N. et al. GLYCAM06: a generalizable biomolecular force field. *Carbohydr. J. Comput. Chem.* **29**, 622–655 (2007).
74. Wang, J., Wang, W., Kollman, P. A. & Case, D. A. Automatic atom type and bond type perception in molecular mechanical calculations. *J. Mol. Graph Model* **25**, 247–260 (2006).
75. Wang, J., Wolf, R. M., Caldwell, J. W., Kollman, P. A. & Case, D. A. Development and testing of a general amber force field. *J. Comput. Chem.* **25**, 1157–1174 (2004).
76. Case, D. A. et al. AmberTools. *J. Chem. Inf. Model.* **63**, 6183–6191 (2023).
77. Jorgensen, W. L., Chandrasekhar, J., Madura, J. D., Impey, R. W. & Klein, M. L. Comparison of simple potential functions for simulating liquid water. *J. Chem. Phys.* **79**, 926–935 (1983).

78. Price, D. J. & Brooks, C. L. III A modified TIP3P water potential for simulation with Ewald summation. *J. Chem. Phys.* **121**, 10096–10103 (2004).
79. Davidchack, R. L., Handel, R. & Tretyakov, M. V. Langevin thermostat for rigid body dynamics. *J. Chem. Phys.* **130**, 234101 (2009).
80. Darden, T., York, D. & Pedersen, L. Particle mesh Ewald: an N·log(N) method for Ewald sums in large systems. *J. Chem. Phys.* **98**, 10089–10092 (1993).
81. Ryckaert, J.-P., Ciccotti, G. & Berendsen, H. J. C. Numerical integration of the cartesian equations of motion of a system with constraints: molecular dynamics of n-alkanes. *J. Comput. Phys.* **23**, 327–341 (1977).
82. Kühne, T. D. et al. CP2K: an electronic structure and molecular dynamics software package - Quickstep: efficient and accurate electronic structure calculations. *J. Chem. Phys.* **152**, 194103 (2020).
83. Tribello, G. A., Bonomi, M., Branduardi, D., Camilloni, C. & Bussi, G. PLUMED 2: new feathers for an old bird. *Comput. Phys. Commun.* **185**, 604–613 (2014).
84. Wan, S., Sinclair, R. C. & Coveney, P. V. Uncertainty quantification in classical molecular dynamics. *Philos. Trans. A Math. Phys. Eng. Sci.* **379**, 20200082 (2021).
85. Perdew, J. P., Burke, K. & Ernzerhof, M. Generalized gradient approximation made simple. *Phys. Rev. Lett.* **77**, 3865–3868 (1996).
86. Calvelo, M. et al. Human O-GlcNAcase uses a preactivated boat-skew substrate conformation for catalysis. Evidence from X-ray crystallography and QM/MM metadynamics. *ACS Catal.* **13**, 13672–13678 (2023).
87. Weigend, F. Accurate Coulomb-fitting basis sets for H to Rn. *Phys. Chem. Chem. Phys.* **8**, 227–236 (2006).
88. Goedecker, S., Teter, M. & Hutter, J. Separable dual-space Gaussian pseudopotentials. *Phys. Rev. B* **54**, 1703–1710 (1996).
89. Cremer, D. & Pople, J. A. General definition of ring puckering coordinates. *J. Am. Chem. Soc.* **97**, 1354–1358 (1975).
90. Ensing, B., Laio, A., Parrinello, M. & Klein, M. L. A Recipe for the computation of the free energy barrier and the lowest free energy path of concerted reactions. *J. Phys. Chem. B* **109**, 6676–6687 (2005).
91. Marcos-Alcalde, I., López-Viñas, E. & Gómez-Puertas, P. MEPSAnd: minimum energy path surface analysis over n-dimensional surfaces. *Bioinformatics* **36**, 956–958 (2020).
92. Humphrey, W., Dalke, A. & Schulten, K. VMD—visual molecular dynamics. *J. Mol. Graph.* **14**, 33–38 (1996).
93. Lu, T. & Chen, F. Multiwfn: a multifunctional wavefunction analyzer. *J. Comput. Chem.* **33**, 580–592 (2012).
94. Lu, T. A comprehensive electron wavefunction analysis toolbox for chemists, Multiwfn. *J. Chem. Phys.* **161**, 082503 (2024).

Acknowledgements

This work was supported by the Spanish Ministry of Science, Innovation and Universities (PID2022-136362NB-I00 to R.H.-G., PID2022-137973NB-I00 to P.M. and PID2023-153181OB-I00 to N.C.R.), Gobierno de Aragón (E34_R17 and LMP58_18) with FEDER (2014–2020) funds for "Building Europe from Aragón" for financial support (to R.H.-G.), and the Danish National Research Foundation (DNRF107 and DNRF196), the Novo Nordisk Foundation (NNF24OC0088218 to Y.N.). The Spanish Ministry of Science, Innovation and Universities is also acknowledged for a pre-doctoral contract to I.S.-M. We thank the ALBA (Barcelona, Spain) synchrotron beamline XALOC. Resources from the supercomputers "Agustina" (provided by BIFI-ZCAM, University of Zaragoza, Spain) are gratefully acknowledged.

Author contributions

Y.N. and S.F. generated the mutants in HEK293 to analyze *At*FUT11 activity. V.T. and M.B.-G. expressed and purified *At*FUT11. V.T. crystallized *At*FUT11 and R.H.-G. solved and built the crystal structure. S.S. and N.C.R. performed the array and mass-spec experiments. I.S.-M. and P.M. performed computational calculations. R.H.-G., I.S.-M., P.M., and H.C. wrote the manuscript, and all authors edited and approved the final version.

Competing interests

The authors declare no competing interests.

Additional information

Supplementary information The online version contains supplementary material available at https://doi.org/10.1038/s41467-026-68786-6.

Correspondence and requests for materials should be addressed to Pedro Merino or Ramon Hurtado-Guerrero.

Peer review information *Nature Communications* thanks Richard Cummings, Shutong Xu, and the other, anonymous, reviewer for their contribution to the peer review of this work. A peer review file is available.